

# Molecular dynamics simulations of heat transport using machine-learned potentials: A mini-review and tutorial on GPUMD with neuroevolution potentials

Cite as: J. Appl. Phys. **135**, 161101 (2024); doi: [10.1063/5.0200833](https://doi.org/10.1063/5.0200833)

Submitted: 29 January 2024 · Accepted: 10 April 2024 ·

Published Online: 24 April 2024



Haikuan Dong,<sup>1,a)</sup> Yongbo Shi,<sup>1</sup> Penghua Ying,<sup>2</sup> Ke Xu,<sup>3</sup> Ting Liang,<sup>3</sup> Yanzhou Wang,<sup>4</sup> Zezhu Zeng,<sup>5</sup> Xin Wu,<sup>6</sup> Wenjiang Zhou,<sup>7,8</sup> Shiyun Xiong,<sup>9</sup> Shunda Chen,<sup>10,a)</sup> and Zheyong Fan<sup>1,a)</sup>

## AFFILIATIONS

<sup>1</sup>College of Physical Science and Technology, Bohai University, Jinzhou, People's Republic of China

<sup>2</sup>Department of Physical Chemistry, School of Chemistry, Tel Aviv University, Tel Aviv 6997801, Israel

<sup>3</sup>Department of Electronic Engineering and Materials Science and Technology Research Center, The Chinese University of Hong Kong, Shatin, N.T. 999077, Hong Kong, People's Republic of China

<sup>4</sup>MSP group, QTF Centre of Excellence, Department of Applied Physics, Aalto University, FI-00076 Aalto, Espoo, Finland

<sup>5</sup>The Institute of Science and Technology Austria, Am Campus 1, 3400 Klosterneuburg, Austria

<sup>6</sup>Department of Engineering Mechanics, School of Civil Engineering and Transportation, South China University of Technology, Guangzhou, Guangdong Province 510640, People's Republic of China

<sup>7</sup>Department of Energy and Resources Engineering, Peking University, Beijing 100871, China

<sup>8</sup>School of Advanced Engineering, Great Bay University, Dongguan 523000, China

<sup>9</sup>Guangzhou Key Laboratory of Low-Dimensional Materials and Energy Storage Devices, School of Materials and Energy, Guangdong University of Technology, Guangzhou 510006, People's Republic of China

<sup>10</sup>Department of Civil and Environmental Engineering, George Washington University, Washington, DC 20052, USA

**Note:** This paper is part of the special topic, Machine Learning for Thermal Transport.

**a) Authors to whom correspondence should be addressed:** [donghaikuan@163.com](mailto:donghaikuan@163.com); [phychensd@gmail.com](mailto:phychensd@gmail.com); and [brucenju@gmail.com](mailto:brucenju@gmail.com)

## ABSTRACT

Molecular dynamics (MD) simulations play an important role in understanding and engineering heat transport properties of complex materials. An essential requirement for reliably predicting heat transport properties is the use of accurate and efficient interatomic potentials. Recently, machine-learned potentials (MLPs) have shown great promise in providing the required accuracy for a broad range of materials. In this mini-review and tutorial, we delve into the fundamentals of heat transport, explore pertinent MD simulation methods, and survey the applications of MLPs in MD simulations of heat transport. Furthermore, we provide a step-by-step tutorial on developing MLPs for highly efficient and predictive heat transport simulations, utilizing the neuroevolution potentials as implemented in the GPUMD package. Our aim with this mini-review and tutorial is to empower researchers with valuable insights into cutting-edge methodologies that can significantly enhance the accuracy and efficiency of MD simulations for heat transport studies.

© 2024 Author(s). All article content, except where otherwise noted, is licensed under a Creative Commons Attribution (CC BY) license (<https://creativecommons.org/licenses/by/4.0/>). <https://doi.org/10.1063/5.0200833>

27 April 2024 04:45:50

## I. INTRODUCTION

Heat transport properties are crucial for numerous applications.<sup>1,2</sup> At the atomistic level, there are primarily three computational methods for heat transport:<sup>3</sup> molecular dynamics (MD) simulations, methods related to Boltzmann transport equation (BTE)—including, more generally, quasi-harmonic Green-Kubo (QHKG) method<sup>4</sup> and Wigner transport equation (WTE) approach<sup>5,6</sup>—combined with anharmonic lattice dynamics (ALD) (BTE-ALD for short), and atomistic Green function (AGF). Each method has its advantages and disadvantages.<sup>3</sup> This mini-review and tutorial focuses on the MD methods. For the BTE-ALD and AGF approaches, we refer interested readers to previous tutorials.<sup>3,7,8</sup> Our emphasis is on thermal conductivity, including finite systems, instead of thermal boundary conductance/resistance. For the latter, we suggest referring to a previous tutorial<sup>9</sup> and a review article.<sup>10</sup>

Notable advantages distinguish MD from the other two methods. First, MD can capture phonon-phonon scatterings at any order, while the other two methods are perturbative in nature and often consider only three-phonon scatterings (for BTE-ALD) or even completely ignore anharmonicity (for AGF). Second, MD can naturally capture scatterings of phonons by other sources such as defects and mass disorder, extending its applicability to fluid systems that are beyond the reach of the other two methods. Third, the computational cost of MD with classical potentials is usually linear with respect to the number of atoms, while it typically exhibits high-order polynomial scaling in the other two methods. Based on these considerations, MD proves particularly suitable for studying heat transport in strongly anharmonic or highly disordered systems.

Despite these advantages, MD simulations have grappled with challenges, particularly in terms of accuracy, over a considerable period of time. The predictive power of MD simulations is highly dependent on the accuracy of the classical potentials, which are mathematical models representing the potential energy surface of systems in terms of geometric information. The interatomic forces can be accurately computed using *ab initio* methods such as quantum-mechanical density-functional theory (DFT), leading to the *ab initio* molecular dynamics (AIMD) method, which has been applied to heat transport studies.<sup>11–14</sup> A challenge in the AIMD approach is the high computational intensity, which imposes limitations on the size and timescales that can be effectively simulated.

Recently, a type of classical potentials based on machine learning (ML) techniques, called machine-learned potentials (MLPs), has emerged as an effective framework for constructing highly accurate interatomic potentials. Due to the flexible functional forms and a large number of fitting parameters in MLPs, they can usually achieve significantly higher accuracy compared to traditional empirical potentials. Notable MLP models, to name a few, include Behler-Parrinello neural-network potential (BPNNP),<sup>15</sup> Gaussian approximation potential (GAP) and related,<sup>16–18</sup> spectral neighbor analysis potential (SNAP),<sup>19</sup> moment tensor potential (MTP),<sup>20</sup> deep potential (DP),<sup>21</sup> and atomic cluster expansion (ACE).<sup>22</sup> In this context, the recently developed neuroevolution potential (NEP) approach<sup>23–25</sup> simultaneously demonstrates excellent accuracy and outstanding computational efficiency, offering a distinctive advantage. Furthermore, MLPs have been increasingly used in MD simulations, including heat transport simulations (see Fig. 1 for a general trend).

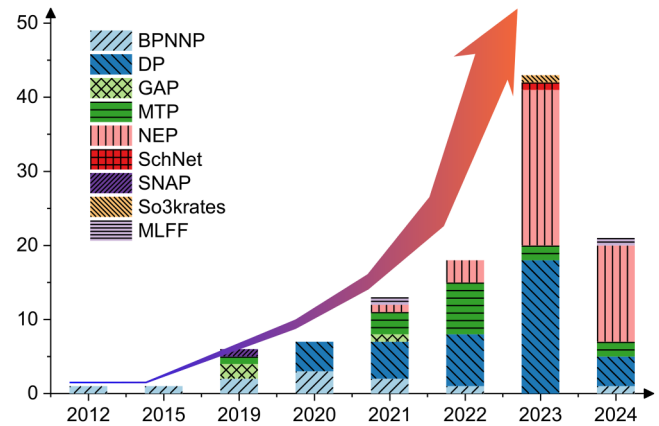


FIG. 1. Number of publications (up to March 10, 2024) on heat transport MD simulations using MLPs as a function of year, with detailed information in Tables I and II.

Parallelization stands out as another key advancement in MD simulations, involving the deployment of parallel computing to take advantage of rapid hardware upgrades and speedups, where a large number of processors or cores work simultaneously to perform calculations, to augment computational efficiency and spatiotemporal scales of simulations. GPUMD,<sup>26</sup> short for Graphics Processing Units Molecular Dynamics, represents a noteworthy development in this arena. GPUMD is a versatile MD package fully implemented on graphics processing units (GPUs). This advancement facilitates the simulations of larger and more complex systems by leveraging the powerful parallel processing capabilities of GPUs. For example, it has been demonstrated that GPUMD can achieve a remarkable computational speed of  $1.5 \times 10^8$  atom step/s (equivalent to a cost of  $6.7 \times 10^{-9}$  s/atom/step) in MD simulations using eight 80-gigabyte A100 graphics cards, enabling simulations up to 100 million atoms for high-entropy alloys employing a general-purpose unified NEP machine-learned potential for 16 elemental metals and their alloys.<sup>27</sup>

In this mini-review and tutorial, we dig into the fundamentals of heat transport, the relevant MD simulation methods, and the applications of MLPs in MD simulations of heat transport. We use the NEP model<sup>23–25</sup> as implemented in the GPUMD package<sup>26</sup> to illustrate the various technical details involved. By completing this tutorial, the readers will gain both fundamental knowledge and practical skills to construct MLPs and apply them in highly efficient and predictive MD simulations of heat transport.

## II. FUNDAMENTALS OF HEAT TRANSPORT AND RELEVANT MD SIMULATION METHODS

### A. Thermal conductivity and thermal conductance

#### 1. Thermal conductivity

Fourier's law describes the empirical relationship governing heat transport, expressed as

$$Q_{\mu} = - \sum_{\nu} \kappa_{\mu\nu} \frac{\partial T}{\partial x_{\nu}}. \quad (1)$$

27 April 2024 04:45:50

**TABLE I.** The MLPs and their implementation packages that have been used in MD simulations of heat transport.

Year	MLP	Package	Code repository or official website
2007	BPNNP	RUNNER	<a href="https://theochemgoettingen.gitlab.io/RuNNer">https://theochemgoettingen.gitlab.io/RuNNer</a>
		AENET	<a href="https://github.com/atomisticnet/aenet">https://github.com/atomisticnet/aenet</a>
		KLIFF	<a href="https://github.com/openkim/kliff">https://github.com/openkim/kliff</a>
2010	GAP	QUIP	<a href="https://github.com/libAtoms/QUIP">https://github.com/libAtoms/QUIP</a>
2015	SNAP	FITSNAP	<a href="https://github.com/FitsSNAP/FitsSNAP">https://github.com/FitsSNAP/FitsSNAP</a>
2016	MTP	MLIP	<a href="https://gitlab.com/ashapeev/mlip-2">https://gitlab.com/ashapeev/mlip-2</a>
2017	SchNet	SCHNETPACK	<a href="https://github.com/atomistic-machine-learning/schnetpack">https://github.com/atomistic-machine-learning/schnetpack</a>
2018	DP	DEEPM-D-KIT	<a href="https://github.com/deepmodeling/deepmd-kit">https://github.com/deepmodeling/deepmd-kit</a>
2019	MLFF	VASP	<a href="https://www.vasp.at">https://www.vasp.at</a>
2021	NEP	GPUMD	<a href="https://github.com/brucefan1983/GPUMD">https://github.com/brucefan1983/GPUMD</a>
2024	So3krates	MLFF	<a href="https://github.com/thorben-frank/mlff">https://github.com/thorben-frank/mlff</a>

Here,  $Q_\mu$  is the heat flux in the  $\mu$  direction,  $\frac{\partial T}{\partial x_\nu}$  is the temperature gradient in the  $\nu$  direction, and  $\kappa_{\mu\nu}$  is an element of the second-rank conductivity tensor.<sup>28</sup> The heat flux measures the heat transport per unit time and per unit area, typically measured in  $\text{W m}^{-2}$ . The thermal conductivity is commonly expressed in units of  $\text{W m}^{-1} \text{K}^{-1}$ .

When the coordinate axes align with the principal axes of the conductivity tensor, thermal transport decouples in different directions, yielding a diagonal thermal conductivity tensor with three nonzero elements:  $\kappa_{xx}$ ,  $\kappa_{yy}$ , and  $\kappa_{zz}$ . These are commonly denoted as  $\kappa_x$ ,  $\kappa_y$ , and  $\kappa_z$  for simplicity. For isotropic 3D systems, we usually define a conductivity scalar  $\kappa$  in terms of the trace of the tensor:  $\kappa = (\kappa_x + \kappa_y + \kappa_z)/3$ . For isotropic 2D systems, we usually define a conductivity scalar for the planar components:  $\kappa = (\kappa_x + \kappa_y)/2$ . For quasi-1D systems, it is only meaningful to define the conductivity in a single direction. For simplicity, from here on we work with the conductivity scalar  $\kappa$  unless it is necessary to consider the conductivity tensor.

## 2. Thermal conductance

In macroscopic transport (the meaning of which will become clear soon), thermal conductance  $K$  is related to thermal conductivity by

$$K = \kappa \frac{A}{L}, \quad (2)$$

where  $A$  is the cross-sectional area and  $L$  is the system length along the transport direction. This relation is similar to that between electrical conductance and electrical conductivity one learns in high school. Usually, thermal conductivity is considered an intrinsic property of a material, and thermal conductance depends on the geometry ( $A$  and  $L$ ). However, complexities emerge when examining heat transport at the nanoscale or mesoscale.

At the nanoscale, the conventional concept of conductivity may lose its validity.<sup>29</sup> For example, thermal transport in materials with high thermal conductivity, such as diamond at the nanoscale, is almost *ballistic*, meaning the conductance changes little with increasing system length  $L$ . In this case, if we assume that Eq. (2)

still holds, then the thermal conductivity  $\kappa$  cannot be regarded as a constant but as a function of the system length,  $\kappa = \kappa(L)$ . This deviates from the conventional (macroscopic) concept of thermal conductivity.

Rather than adhering strictly to Eq. (2), one can generalize the relation between conductance and conductivity as follows:

$$\frac{1}{K} = \frac{1}{K_0} + \frac{1}{\kappa A}, \quad (3)$$

where  $K_0$  is the ballistic thermal conductance of the material. The term  $\kappa$  in Eq. (3) refers to the *diffusive thermal conductivity*, the conventional thermal conductivity defined in the macroscopic limit ( $L \rightarrow \infty$ ) where the phonon transport is diffusive. By contrast, the length-dependent thermal conductivity  $\kappa(L)$  defined in Eq. (2) is usually called the *apparent thermal conductivity* or *effective thermal conductivity*. In the diffusive limit, the apparent thermal conductivity  $\kappa(L)$  defined in Eq. (2) approaches the diffusive conductivity  $\kappa$  defined in Eq. (3), as expected.

By comparing Eqs. (2) and (3), we obtain the following relation between the apparent thermal conductivity  $\kappa(L)$  and the diffusive thermal conductivity  $\kappa$ :

$$\frac{1}{\kappa(L)} \frac{L}{A} = \frac{1}{K_0} + \frac{1}{\kappa A}. \quad (4)$$

From this, we have

$$\frac{1}{\kappa(L)} = \frac{1}{\kappa} \left( 1 + \frac{\kappa A}{K_0 L} \right). \quad (5)$$

It is more common to use thermal conductance per unit area  $G$ , which is defined as

$$G \equiv \frac{K}{A}. \quad (6)$$

The corresponding ballistic conductance per unit area is

27 April 2024 04:45:50

TABLE II. Applications of MLPs in MD simulations of heat transport up to March 10, 2024.

MLP	Year	Reference	Material(s)	Year	Reference	Material(s)
BPNNP	2012	Sosso <sup>64</sup>	Amorphous GeTe	2015	Campi <sup>65</sup>	GeTe
	2019	Bosoni <sup>66</sup>	GeTe nanowires	2019	Wen <sup>67</sup>	2D graphene
	2020	Cheng <sup>68</sup>	Liquid hydrogen	2020	Mangold <sup>69</sup>	Mn <sub>x</sub> Ge <sub>y</sub>
	2020	Shimamura <sup>37</sup>	Ag <sub>2</sub> Se	2021	Han <sup>70</sup>	Sn
	2021	Shimamura <sup>71</sup>	Ag <sub>2</sub> Se	2022	Takeshita <sup>72</sup>	Ag <sub>2</sub> Se
GAP	2024	Shimamura <sup>73</sup>	Ag <sub>2</sub> Se			
	2019	Qian <sup>74</sup>	Silicon	2019	Zhang <sup>75</sup>	2D silicene
SNAP	2021	Zeng <sup>76</sup>	Tl <sub>3</sub> VSe <sub>4</sub>			
	2019	Gu <sup>77</sup>	MoS <sub>2</sub> alloy			
MTP	2019	Korotaev <sup>78</sup>	CoSb <sub>3</sub>	2021	Liu <sup>79</sup>	SnSe
	2021	Yang <sup>80</sup>	CoSb <sub>3</sub> and Mg <sub>3</sub> Sb <sub>2</sub>	2021	Zeng <sup>81</sup>	BaAg <sub>2</sub> Te <sub>2</sub>
	2022	Attarian <sup>82</sup>	FLiBe	2022	Ouyang <sup>83</sup>	SnS
	2022	Ouyang <sup>84</sup>	BA <sub>s</sub> and Diamond	2022	Mortazavi <sup>85–87</sup>	Graphyne, 2D BCN, C <sub>60</sub>
	2022	Sun <sup>88</sup>	Bi <sub>2</sub> O <sub>2</sub> Se	2023	Mortazavi <sup>89–91</sup>	C <sub>60</sub> , C <sub>36</sub> and B <sub>40</sub> networks
SchNet	2023	Wang <sup>92</sup>	Cs <sub>2</sub> AgPdCl <sub>5</sub> etc.	2023	Zhu <sup>93</sup>	CuSe
	2024	Chang <sup>94</sup>	PbSnTeSe and PbSnTeS	2024	Wieser <sup>95</sup>	MOF crystals
DP	2023	Langer <sup>41</sup>	ZrO <sub>2</sub>			
	2020	Dai <sup>96</sup>	ZrHfTiNbTaC alloy	2020	Li <sup>97</sup>	$\beta$ -Ga <sub>2</sub> O <sub>3</sub>
	2020	Li <sup>98</sup>	Silicon	2020	Pan <sup>99</sup>	ZnCl <sub>2</sub>
	2021	Bu <sup>100</sup>	KCl-CaCl <sub>2</sub> molten salt	2021	Dai <sup>101</sup>	TiZrHfNbTaB alloy
	2021	Deng <sup>102</sup>	MgSiO <sub>3</sub> liquid	2021	Liu <sup>103</sup>	Al
	2021	Tisi <sup>35</sup>	Water	2022	Gputa <sup>104</sup>	Cu <sub>7</sub> PSe <sub>6</sub>
	2022	Huang <sup>105</sup>	B <sub>12</sub> P <sub>2</sub>	2022	Liang <sup>106</sup>	MgCl <sub>2</sub> -NaCl eutectic
	2022	Pegolo <sup>107</sup>	Li <sub>3</sub> ClO	2022	Wang <sup>108</sup>	Wadsleyite
	2022	Yang <sup>109</sup>	MgSiO <sub>3</sub> perovskite	2022	Zhang <sup>110</sup>	Bi <sub>2</sub> Te <sub>3</sub>
	2023	Bhatt <sup>111</sup>	Tungsten	2023	Dong <sup>112</sup>	NaCl-MgCl <sub>2</sub> -CaCl <sub>2</sub>
	2023	Fu <sup>113</sup>	Ti-Zr-Y-Si-O ceramic	2023	Gupta <sup>114</sup>	Bulk MoSe <sub>2</sub> and WSe <sub>2</sub>
	2023	Han <sup>115</sup>	2D InSe	2023	Huang <sup>116</sup>	CdTe
	2023	Li <sup>117,118</sup>	Cu/H <sub>2</sub> O and TiO <sub>2</sub> /H <sub>2</sub> O	2023	Qi <sup>119</sup>	Vitreous silica
	2023	Qiu <sup>120</sup>	Ice	2023	Qu <sup>121</sup>	MnBi <sub>2</sub> Te <sub>4</sub> , Bi <sub>2</sub> Te <sub>3</sub> /MnBi <sub>2</sub> Te <sub>4</sub>
	2023	Ren <sup>122</sup>	Ag <sub>8</sub> SnSe <sub>6</sub>	2023	Wang <sup>123</sup>	Bridgmanite, Post-perovskite
	2023	Xu <sup>124</sup>	MgCl <sub>2</sub> -NaCl and MgCl <sub>2</sub> -KCl	2023	Zhang <sup>125,126</sup>	Sb <sub>2</sub> Te <sub>3</sub>
	2023	Zhang <sup>127</sup>	Water	2023	Zhang <sup>128</sup>	Boron arsenide
	2023	Zhao <sup>129</sup>	NaCl and NaCl-SiO <sub>2</sub>	2024	Fu <sup>130</sup>	SiC
	2024	Li <sup>131</sup>	AlN	2024	Li <sup>132</sup>	GaN/SiC interfaces
	2024	Peng <sup>133</sup>	MgSiO <sub>3</sub> -H <sub>2</sub> O	2024	Zhang <sup>134</sup>	MoAlB
MLFF	2021	Verdi <sup>135</sup>	ZrO <sub>2</sub>	2024	Lahnsteiner <sup>136</sup>	CsPbBr <sub>3</sub>
	2021	Fan <sup>23</sup>	PbTe, Si	2022	Dong <sup>137</sup>	2D silicene
NEP	2022	Fan <sup>24,25</sup>	PbTe, Amorphous carbon	2023	Cheng <sup>138</sup>	PbTe
	2023	Dong <sup>139</sup>	C <sub>60</sub> network	2023	Du <sup>140</sup>	PH <sub>4</sub> AlBr <sub>4</sub>
	2023	Eriksson <sup>141</sup>	Graphite, <i>h</i> -BN, MoS <sub>2</sub>	2023	Liang <sup>142</sup>	Amorphous SiO <sub>2</sub>
	2023	Liu <sup>143</sup>	Si/Ge nanowires	2023	Lu <sup>144</sup>	Fullerene-encapsulated CNT
	2023	Ouyang <sup>145</sup>	AgX (X=Cl, Br, I)	2023	Pan <sup>146</sup>	MgOH system
	2023	Sha <sup>147</sup>	2D PbTe	2023	Shi <sup>148</sup>	InGeX <sub>3</sub> (X=S, Se, Te)
	2023	Shi <sup>149</sup>	Halogen perovskites	2023	Su <sup>150</sup>	Cs <sub>2</sub> BiAgBr <sub>6</sub> , Cs <sub>2</sub> BiAgCl <sub>6</sub>
	2023	Sun <sup>151</sup>	Ga <sub>2</sub> O <sub>3</sub>	2023	Wang <sup>152</sup>	Amorphous silicon
	2023	Wang <sup>153</sup>	2D SrTiO <sub>3</sub>	2023	Xu <sup>154</sup>	Water
	2023	Xiong <sup>155</sup>	Diamond allotropes	2023	Ying <sup>156,157</sup>	MOF crystals, Phosphorene
	2023	Zhang <sup>158</sup>	Amorphous HfO <sub>2</sub>	2024	Cao <sup>159</sup>	Phosphorous carbide
	2024	Cheng <sup>160</sup>	Perovskites	2024	Fan <sup>161</sup>	HKUST-1 crystal
	2024	Fan <sup>162</sup>	Graphene antidot lattice	2024	Li <sup>163</sup>	Strained monolayer graphene
	2024	Li <sup>164</sup>	Amorphous silicon	2024	Li <sup>165</sup>	2D COF-5
	2024	Pegolo <sup>166</sup>	Glassy Li <sub>x</sub> Si <sub>1-x</sub>	2024	Wang <sup>167</sup>	Ga <sub>2</sub> O <sub>3</sub>
	2024	Ying <sup>168</sup>	MOF crystals	2024	Yue <sup>169</sup>	Si-C interfaces
So3krates	2024	Zeraati <sup>170</sup>	La <sub>2</sub> Zr <sub>2</sub> O <sub>7</sub> and many others	2024	Zhang <sup>171</sup>	GeTe
	2023	Langer <sup>42</sup>	SnSe			

27 April 2024 04:45:50

$G_0 = K_0/A$ . Using this, we have

$$\frac{1}{\kappa(L)} = \frac{1}{\kappa} \left( 1 + \frac{\kappa/G_0}{L} \right). \quad (7)$$

The ratio between the diffusive conductivity and the ballistic conductance per unit area defines a phonon mean free path (MFP),

$$\lambda \equiv \frac{\kappa}{G_0}. \quad (8)$$

In terms of the phonon MFP, we have

$$\frac{1}{\kappa(L)} = \frac{1}{\kappa} \left( 1 + \frac{\lambda}{L} \right). \quad (9)$$

This is known as the ballistic-to-diffusive transition formula for the length-dependent thermal conductivity. Figure 2 schematically shows the ballistic-to-diffusive transition behavior.

The above discussion is simplified in the sense that no channel dependence of the thermal transport has been taken into account. Different channels usually have different MFPs and diffusive conductivities. In general, both the conductivity and the MFP are frequency dependent and we can generalize Eq. (9) to

$$\frac{1}{\kappa(\omega, L)} = \frac{1}{\kappa(\omega)} \left( 1 + \frac{\lambda(\omega)}{L} \right). \quad (10)$$

With  $\kappa(\omega, L)$ , we can obtain the apparent thermal conductivity at any length  $L$  as

$$\kappa(L) = \int_0^\infty \frac{d\omega}{2\pi} \kappa(\omega, L). \quad (11)$$

We use two toy models to illustrate the above-discussed concepts. In the first model, we assume that there is only one phonon MFP of  $1\mu\text{m}$  and a diffusive thermal conductivity of  $\kappa = 1000\text{ W m}^{-1}\text{ K}^{-1}$ . Then, ballistic conductance is

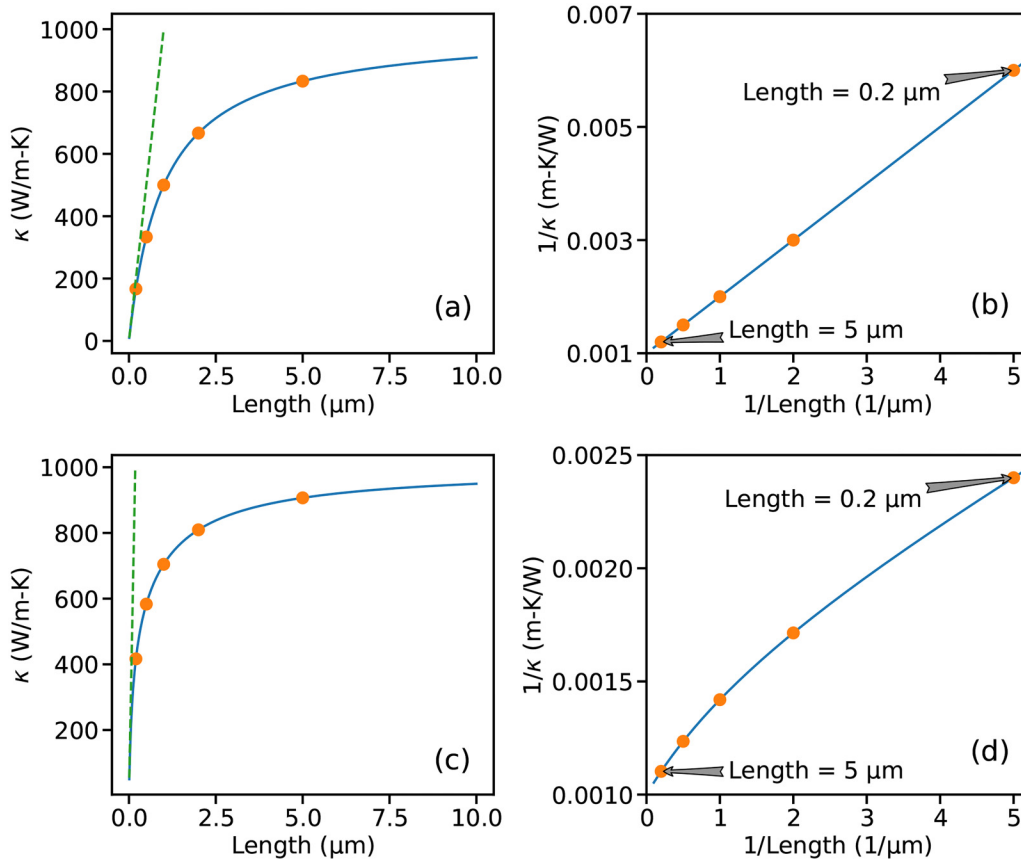


**FIG. 2.** Ballistic-to-diffusive transition of the apparent thermal conductivity  $\kappa(L)$ . (a) and (b) a toy model with a single phonon MFP of  $1\mu\text{m}$  and a diffusive thermal conductivity of  $\kappa = 1000\text{ W/m K}$ ; (c) and (d) a toy model with two phonon MFPs, one of  $0.1\mu\text{m}$ , the other  $1\mu\text{m}$ , with diffusive conductivity of  $500\text{ W/m K}$ . The dots in each panel represent a few special lengths, from 0.2 to  $5\mu\text{m}$ . In (a) and (c), the dashed lines represent the ballistic limit.

27 April 2024 04:45:50

$\kappa/\lambda = 1 \text{ GW m}^{-2} \text{ K}^{-1}$ . Then, the apparent thermal conductivity  $\kappa(L)$  is given by Eq. (9), as shown in Figs. 2(a) and 2(b). In this case,  $1/\kappa(L)$  varies linearly with  $1/L$ . In the second model, we assume that there are two phonon modes, one with a MFP of  $0.1 \mu\text{m}$ , and the other  $1 \mu\text{m}$ , both having a diffusive conductivity of  $500 \text{ W m}^{-1} \text{ K}^{-1}$ . Then the ballistic conductances for these two modes are 5 and  $0.5 \text{ GW m}^{-2} \text{ K}^{-1}$ , respectively. The higher ballistic conductance in the second toy model can be visualized in Fig. 2(c). Although the apparent thermal conductivity for each mode follows Eq. (9), when combined,  $1/\kappa(L)$  does *not* exhibit linearity with  $1/L$ . This is an important feature for realistic materials with a general MFP spectrum  $\kappa(\omega)$ .

## B. Heat flux and heat current

The heat flux is defined as the time derivative of the sum of the moments of the site energies of the particles in the system,<sup>30</sup>

$$\mathbf{Q} \equiv \frac{1}{V} \frac{d}{dt} \sum_i \mathbf{r}_i E_i. \quad (12)$$

The site energy  $E_i$  is the sum of the kinetic energy  $m_i \mathbf{v}_i^2/2$  and the potential energy  $U_i$ . Here  $m_i$ ,  $\mathbf{r}_i$ , and  $\mathbf{v}_i$  are the mass, position, and velocity of particle  $i$ , respectively, and  $V$  is the controlling volume for the particles, which is usually the volume of the simulation box, but can also be specifically defined for low-dimensional systems simulated with vacuum layers. In MD simulations, it is usually more convenient to work on the heat current that is an extensive quantity,

$$\mathbf{J} \equiv V \mathbf{Q}. \quad (13)$$

It is clear that the total heat current can be written as two terms,

$$\mathbf{J} = \mathbf{J}_{\text{kin}} + \mathbf{J}_{\text{pot}}, \quad (14)$$

where the first term is the kinetic or convective part,

$$\mathbf{J}_{\text{kin}} = \sum_i \mathbf{v}_i E_i \quad (15)$$

and the second term is called the potential part,

$$\mathbf{J}_{\text{pot}} = \sum_i \mathbf{r}_i (\mathbf{F}_i \cdot \mathbf{v}_i) + \sum_i \mathbf{r}_i \frac{dU_i}{dt}. \quad (16)$$

The expression above involves absolute positions and is thus not directly applicable to periodic systems. To derive an expression that can be used for periodic systems, we need to discuss potential energy and interatomic force first.

For the MLPs discussed in this tutorial, the total potential energy  $U$  of a system can be written as the sum of site potentials  $U_i$ ,

$$U = \sum_{i=1}^N U_i. \quad (17)$$

The site potential can have different forms in different potential models. A well-defined force expression for general many-body potentials that explicitly respects Newton's third law has been derived as<sup>31</sup>

$$\mathbf{F}_i = \sum_{j \neq i} \mathbf{F}_{ij}, \quad (18)$$

where

$$\mathbf{F}_{ij} = -\mathbf{F}_{ji} = \frac{\partial U_i}{\partial \mathbf{r}_{ij}} - \frac{\partial U_j}{\partial \mathbf{r}_{ji}}. \quad (19)$$

Here,  $\partial U_i / \partial \mathbf{r}_{ij}$  is a shorthand notation for a vector with Cartesian components  $\partial U_i / \partial x_{ij}$ ,  $\partial U_i / \partial y_{ij}$ , and  $\partial U_i / \partial z_{ij}$ . The atomic position difference is defined as

$$\mathbf{r}_{ij} \equiv \mathbf{r}_j - \mathbf{r}_i. \quad (20)$$

Using the force expression, the heat current can be derived to be<sup>31</sup>

$$\mathbf{J}_{\text{pot}} = \sum_i \sum_{j \neq i} \mathbf{r}_{ij} \left( \frac{\partial U_j}{\partial \mathbf{r}_{ji}} \cdot \mathbf{v}_i \right). \quad (21)$$

From the definition of virial tensor

$$\mathbf{W} = \sum_i \mathbf{W}_i = \sum_i \mathbf{r}_i \otimes \mathbf{F}_i \quad (22)$$

and the force expression Eq. (18), we have

$$\mathbf{W} = -\frac{1}{2} \sum_i \sum_{j \neq i} \mathbf{r}_{ij} \otimes \mathbf{F}_{ij}. \quad (23)$$

Using the explicit force expression Eq. (19), we can also express the per-atom virial as

$$\mathbf{W}_i = \sum_{j \neq i} \mathbf{r}_{ij} \otimes \frac{\partial U_j}{\partial \mathbf{r}_{ji}}. \quad (24)$$

Therefore, the heat current can be neatly written as

$$\mathbf{J}_{\text{pot}} = \sum_i \mathbf{W}_i \cdot \mathbf{v}_i. \quad (25)$$

This expression, which involves relative atom positions only, is applicable to periodic systems and has been implemented in the GPUMD package<sup>26</sup> for all the supported interatomic potentials, including NEP. The current implementation of the heat current in LAMMPS<sup>32</sup> is generally incorrect for many-body potentials, and corrections to LAMMPS have only been done for special force fields.<sup>33,34</sup> For any MLP that interfaces with LAMMPS, one must use the full nine components of the per-atom virial and provide a correct implementation of Eq. (24). NEP has an interface for LAMMPS that meets this requirement. To the best of our knowledge, among the other publicly available MLP packages, only DEEPM<sup>21</sup> (after the



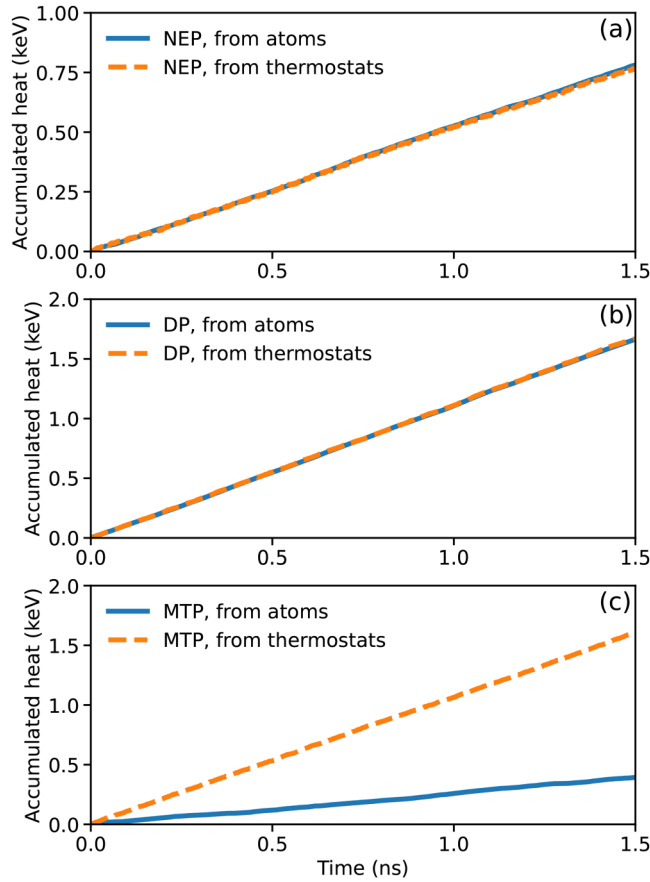


**FIG. 3.** Accumulated heat as a function of time in non-equilibrium steady state simulated with (a) NEP, (b) DP, and (c) MTP, using GPUMD<sup>26</sup> (for NEP) or LAMMPS<sup>32</sup> (for DP and MTP).

work of Tisi *et al.*<sup>35</sup>) and AENET<sup>36</sup> (after the work of Shimamura *et al.*<sup>37</sup>) have implemented the heat current correctly. The heat current is also correctly formulated<sup>38</sup> for a MLP based on the smooth overlap of atomic positions.<sup>39</sup> Contrarily, the widely used MTP method<sup>20</sup> (as implemented in Ref. 40), for example, exhibits an incorrect implementation of the heat current, as demonstrated in Fig. 3. According to energy conservation, the accumulated heat from the atoms [cf. Eq. (25)] should match that from the thermostats [cf. Eq. (31)], allowing for only small fluctuations. It is evident that both DP and NEP exhibit this property, whereas MTP does not. Details on the calculations are provided in the Appendix.

Note that the above formulation of heat current has been derived specifically for *local* MLPs with atom-centered descriptors. For *semilocal* message-passing-based MLPs, the formulation of heat current has been shown by Langer *et al.*<sup>41,42</sup> to be more complicated.

### C. Overview of MD-based methods for heat transport

In the following, we review the heat transport MD methods implemented in the GPUMD package, including equilibrium molecular

dynamics (EMD), nonequilibrium molecular dynamics (NEMD), homogeneous nonequilibrium molecular dynamics (HNEMD), and spectral decomposition. While the approach-to-equilibrium method<sup>43–45</sup> can in principle be realized in GPUMD, our discussion will primarily focus on the other three methods that have been widely employed with GPUMD.

#### 1. The EMD method

The EMD method is based on the Green–Kubo relation for thermal transport,<sup>46</sup>

$$\kappa_{\mu\nu}(t) = \frac{1}{k_B T^2 V} \int_0^t dt' C_{\mu\nu}(t'), \quad (26)$$

where  $C_{\mu\nu}(t)$  is the heat current autocorrelation function (HCACF)

$$C_{\mu\nu}(t) = \langle J_\mu(0) J_\nu(t) \rangle_e. \quad (27)$$

The equations above define the running thermal conductivity, which is a function of the correlation time  $t$ . In MD simulations, the correlation function is defined as

$$\langle J_\mu(0) J_\nu(t) \rangle_e \approx \frac{1}{t_p} \int_0^{t_p} J_\mu(\tau) J_\nu(t + \tau) d\tau. \quad (28)$$

where  $t_p$  is the *production time* within which the heat current data are sampled. This production run should be in an equilibrium ensemble (as indicated by the subscript “e” in the HCACF expression), usually NVE, but NVT with a *global* thermostat can also be used. Thermal conductivity in the diffusive limit is obtained by taking the limit of  $t \rightarrow \infty$ , but in practice, this limit can be well approximated at an appropriate  $t$ . One also needs to ensure that the simulation cell is sufficiently large to eliminate finite-size effects.<sup>47–49</sup>

#### 2. The NEMD method

The NEMD method is a nonequilibrium and inhomogeneous method that involves implementing a pair of heat source and sink using a thermostating method or equivalent. There are two common relative positions of the source and sink in the NEMD method, corresponding to two typical simulation setups. In one setup, the source and sink are separated by half of the simulation cell length  $L$ , and periodic boundary conditions are applied along the transport direction. Heat flows from the source to the sink in two opposite directions in this periodic boundary setup. In the other setup, the source and sink separated by  $L$  are located at the two ends of the system. Fixed boundary conditions are applied along the transport direction to prevent sublimation of the atoms in the heat source and sink. Heat flows from the source to the sink in one direction in this fixed boundary setup. It has been established<sup>50</sup> that the effective length in the periodic boundary setup is only  $L/2$ . This factor must be taken into account when comparing results from the two setups.

When the system reaches a steady state, a temperature profile with a definite temperature gradient  $\nabla T$  will be established. Meanwhile, a steady heat flux  $Q$  will be generated. With these, one

27 April 2024 04:45:50

can obtain the apparent thermal conductivity  $\kappa(L)$  of a system of finite length  $L$  according to Fourier's law,

$$\kappa(L) = \frac{Q}{|\nabla T|}, \quad (29)$$

in the linear response regime where the temperature gradient  $|\nabla T|$  across the system is sufficiently small. It has been observed that the local Langevin thermostat outperforms the global Nosé–Hoover thermostat<sup>51,52</sup> in generating temperature gradients.<sup>53</sup> It has also been demonstrated that the temperature gradient should be directly calculated from the temperature difference  $|\nabla T| = \Delta T/L$  rather than through fitting part of the temperature profile.<sup>53</sup> This is to ensure that the contact resistance is also included, and the total thermal conductance is given by

$$G(L) = \frac{Q}{|\Delta T|}. \quad (30)$$

The steady-state heat flux can be computed either microscopically or from the energy exchange rate  $dE/dt$  in the thermostatted regions and cross-sectional area  $A$  as

$$Q = \frac{1}{A} \frac{dE}{dt}, \quad (31)$$

based on energy conservation. The two approaches must generate the same result, and they have been used to validate the implementation of heat flux in several MLPs, as shown in Fig. 3.

A common practice in using the NEMD method is to extrapolate to the limit of infinite length based on the results for a few finite lengths. It is important to note that linear extrapolation is usually insufficient, as suggested even by the toy-model results shown in Fig. 2(d).

### 3. The HNEMD method

In the HNEMD method, an external force of the form<sup>54</sup>

$$\mathbf{F}_i^{\text{ext}} = E_i \mathbf{F}_e + \mathbf{F}_e \cdot \mathbf{W}_i \quad (32)$$

is added to each atom to drive the system out of equilibrium, inducing a nonequilibrium heat current (note the subscript “ne”),

$$\langle \mathbf{J}(t) \rangle_{\text{ne}} = \left( \frac{1}{k_B T} \int_0^t dt' \langle \mathbf{J}(0) \otimes \mathbf{J}(t') \rangle_e \right) \cdot \mathbf{F}_e. \quad (33)$$

The driving force parameter  $\mathbf{F}_e$  is of the dimension of inverse length. The quantity in the parentheses is proportional to the running thermal conductivity tensor and we have

$$\frac{\langle \mathbf{J}_q^\mu(t) \rangle_{\text{ne}}}{TV} = \sum_v \kappa^{\mu\nu}(t) \mathbf{F}_e^\nu. \quad (34)$$

This provides a way of computing the thermal conductivity. In the HNEMD method, the system is in a homogeneous nonequilibrium state because there is no explicit heat source and sink. The system

is periodic in the transport direction and heat flows circularly under the driving force. Because of the absence of heat source and sink, no boundary scattering occurs for the phonons and the HNEMD method is similar to the EMD method in terms of finite-size effects.

### 4. Spectral decomposition

In the framework of the NEMD and HNEMD methods, one can also calculate spectrally decomposed thermal conductivity (or conductance) using the virial-velocity correlation function,<sup>54,55</sup>

$$K(t) = \left\langle \sum_i \mathbf{W}_i(0) \cdot \mathbf{v}_i(t) \right\rangle_{\text{ne}}. \quad (35)$$

In terms of this, the thermal conductance in NEMD simulation can be decomposed as follows:

$$G = \int_{-\infty}^{+\infty} \frac{d\omega}{2\pi} G(\omega), \quad (36)$$

$$G(\omega) = \frac{2}{V\Delta T} \int_{-\infty}^{+\infty} e^{i\omega t} K^\mu(t) dt. \quad (37)$$

The thermal conductivity in HNEMD simulation can be decomposed as follows:

$$\kappa_{\mu\nu} = \int_{-\infty}^{+\infty} \frac{d\omega}{2\pi} \kappa_{\mu\nu}(\omega), \quad (38)$$

$$\frac{2}{VT} \int_{-\infty}^{+\infty} e^{i\omega t} K^\mu(t) dt = \sum_v \kappa_{\mu\nu}(\omega) \mathbf{F}_e^\nu. \quad (39)$$

The virial-velocity correlation function here is essentially the force-velocity correlation function defined for a (physical or imaginary) interface.<sup>56,57</sup>

The spectral quantities allow for a feasible quantum-statistical correction<sup>5,58</sup> for strongly disordered systems where phonon-phonon scatterings are not dominant. For example, the spectral thermal conductivity can be quantum-corrected by multiplying the factor

$$\frac{x^2 e^x}{(e^x - 1)^2}, \quad (40)$$

where  $x = \hbar\omega/k_B T$ .

There are other spectral/modal analysis method implemented in GPUMD, such as the Green–Kubo modal analysis method<sup>59</sup> and the homogeneous non-equilibrium modal analysis method,<sup>58</sup> but we will not demonstrate their usage in this tutorial.

## III. REVIEW OF MD SIMULATION OF HEAT TRANSPORT USING MLPs

Several MLPs have been used for heat transport with MD simulations, including BPNNP,<sup>15</sup> GAP,<sup>16</sup> SNAP,<sup>19</sup> MTP,<sup>20</sup> DP,<sup>21</sup>

27 April 2024 04:45:50



MLFF,<sup>60</sup> NEP,<sup>23</sup> SchNet,<sup>61</sup> and So3kates.<sup>62</sup> Table I lists the relevant MLP packages implementing these MLPs.

The pioneering BPNP model, developed by Behler and Parrinello,<sup>15</sup> has been implemented in various packages, including RUNNER,<sup>15</sup> AENET,<sup>36</sup> and KLIF.<sup>63</sup> The DP, MLFF, NEP, GAP, MTP, SNAP, SchNet, and So3kates models are implemented in DEEPM-DIT, VASP, GPUMD, QUIP, MLIP, FITSNAP, SCHNETPACK, and MLFF respectively.

Most MLP packages are interfaced to LAMMPS<sup>32</sup> to perform MD simulations, while NEP is native to GPUMD<sup>26</sup> but can also be interfaced to LAMMPS. The MLFF method implemented in VASP is an on-the-fly MLP that integrates seamlessly into AIMD simulations.

Table II compiles the publications up to today that have used MD simulations driven by MLPs for thermal transport studies. Note that our focus is on studies using MD simulations, excluding those solely based on the BTE-ALD approach. The number of publications up to March 10, 2024 for each MLP is shown in Fig. 1.

The application of MLPs-based MD simulations to thermal transport was pioneered by Sosso *et al.* in 2012 when they studied the thermal transport in the phase-changing amorphous GeTe system.<sup>64</sup> However, thermal transport simulations are very computationally intensive, and the rapid increase of the number of applications has only been started after the development of the GPU-based DP<sup>21</sup> and NEP<sup>23</sup> models. In this regard, the NEP model is particularly advantageous due to its superior computational speed as compared to others.<sup>23–25</sup> With comparable computational resources, it has been shown to be as fast as or even faster than some empirical force fields.<sup>154,156</sup>

There are numerous successful applications of MLPs in thermal transport. In Fig. 4, we present results from selected publications. The materials studied in these works have reliable experimental results, serving as good candidates for validating the applicability of MLPs. On one hand, MLPs demonstrate good agreement with experimental results for highly disordered materials such as liquid water,<sup>154</sup> amorphous SiO<sub>2</sub>,<sup>142</sup> and amorphous silicon.<sup>152</sup> In addition to the reliability of MLPs, a crucial component for accurately describing the temperature dependence of the thermal conductivity in liquids and amorphous materials is a quantum correction method based on the spectral thermal conductivity, as defined in Eq. (39), and the quantum-statistical-correction factor, as given in Eq. (40). On the other hand, MLPs tend to systematically underestimate the thermal conductivity of crystalline solids, including silicon (using a GAP model),<sup>74</sup> CoSb<sub>3</sub> (using a MTP model), and graphite (in-plane transport, using a NEP model).<sup>141</sup> This underestimation has been attributed to the small but finite random force errors, and a correction has been devised.<sup>181</sup> We will discuss this in more detail with an example in Sec. IV.

#### IV. MOLECULAR DYNAMICS SIMULATION OF HEAT TRANSPORT USING NEP AND GPUMD

In this section, we use crystalline silicon as an example to demonstrate the workflow of constructing and using NEP models for thermal transport simulations. The NEP approach has been implemented in the open-source GPUMD package.<sup>25,26</sup> After compiling, there will be an executable named `nep` that can be used to

train accurate NEP models against reference data, and an executable named `gpumd` that can be used to perform efficient MD simulations. The GPUMD package is self-contained, free from dependencies on third-party packages, particularly those related to ML. This makes the installation of GPUMD straightforward and effortless. In addition, there are some handy (but not mandatory) Python packages available to facilitate the pre-processing and post-processing GPUMD inputs and outputs, including CALORINE,<sup>182</sup> GPYUMD,<sup>183</sup> GPUMD-WIZARD,<sup>184</sup> and PYNEP.<sup>185</sup> Since its inception with the very first version in 2013,<sup>186</sup> GPUMD has been developed with special expertise in heat transport applications.

#### A. The neuroevolution potential

The NEP model is based on artificial neural network (ANN) and is trained using a separable natural evolution strategy (SNES),<sup>187</sup> hence the name.

##### 1. The NN model

The ML model in NEP is a fully-connected feedforward ANN with a single hidden layer, which is also called a multilayer perceptron. The total energy is the sum of the site energies  $U = \sum_i U_i$ , and the site energy  $U_i$  is the output of the neural network (NN), expressed as

$$U_i = \sum_{\mu=1}^{N_{\text{neu}}} \omega_{\mu}^{(1)} \tanh \left( \sum_{v=1}^{N_{\text{des}}} \omega_{\mu v}^{(0)} q_v^i - b_{\mu}^{(0)} \right) - b^{(1)}. \quad (41)$$

Here,  $N_{\text{des}}$  is the number of descriptor components,  $N_{\text{neu}}$  is the number of neurons in the hidden layer,  $q_v^i$  is the  $v$ -th descriptor component of atom  $i$ ,  $\omega_{\mu v}^{(0)}$  is the connection weight matrix from the input layer to the hidden layer,  $\omega_{\mu}^{(1)}$  is the connection weight vector from the hidden layer to the output layer,  $b_{\mu}^{(0)}$  is the bias vector in the hidden layer, and  $b^{(1)}$  is the bias in the output layer.  $\omega_{\mu v}^{(0)}$ ,  $\omega_{\mu}^{(1)}$ ,  $b_{\mu}^{(0)}$ , and  $b^{(1)}$  are trainable parameters. The function  $\tanh(x)$  is the nonlinear activation function in the hidden layer. According to Eq. (41), the NEP model is a simple analytical function of a descriptor vector. A C++ function for evaluating the energy and its derivative with respect to the descriptor components can be found in Ref. 25.

##### 2. The descriptor

The descriptor  $q_i^v$  encompasses the local environment of atom  $i$ . In NEP, the descriptor is an abstract vector whose components group into radial and angular parts. The radial descriptor components  $q_n^i$  ( $0 \leq n \leq n_{\text{max}}^R$ ) are defined as

$$q_n^i = \sum_{j \neq i} g_n(r_{ij}), \quad (42)$$

where  $r_{ij}$  is the distance between atoms  $i$  and  $j$  and  $g_n(r_{ij})$  are a set of radial functions, each of which is formed by a linear combination of Chebyshev polynomials. The angular components include  $n$ -body ( $n = 3, 4, 5$ ) correlations. For the 3-body part, the

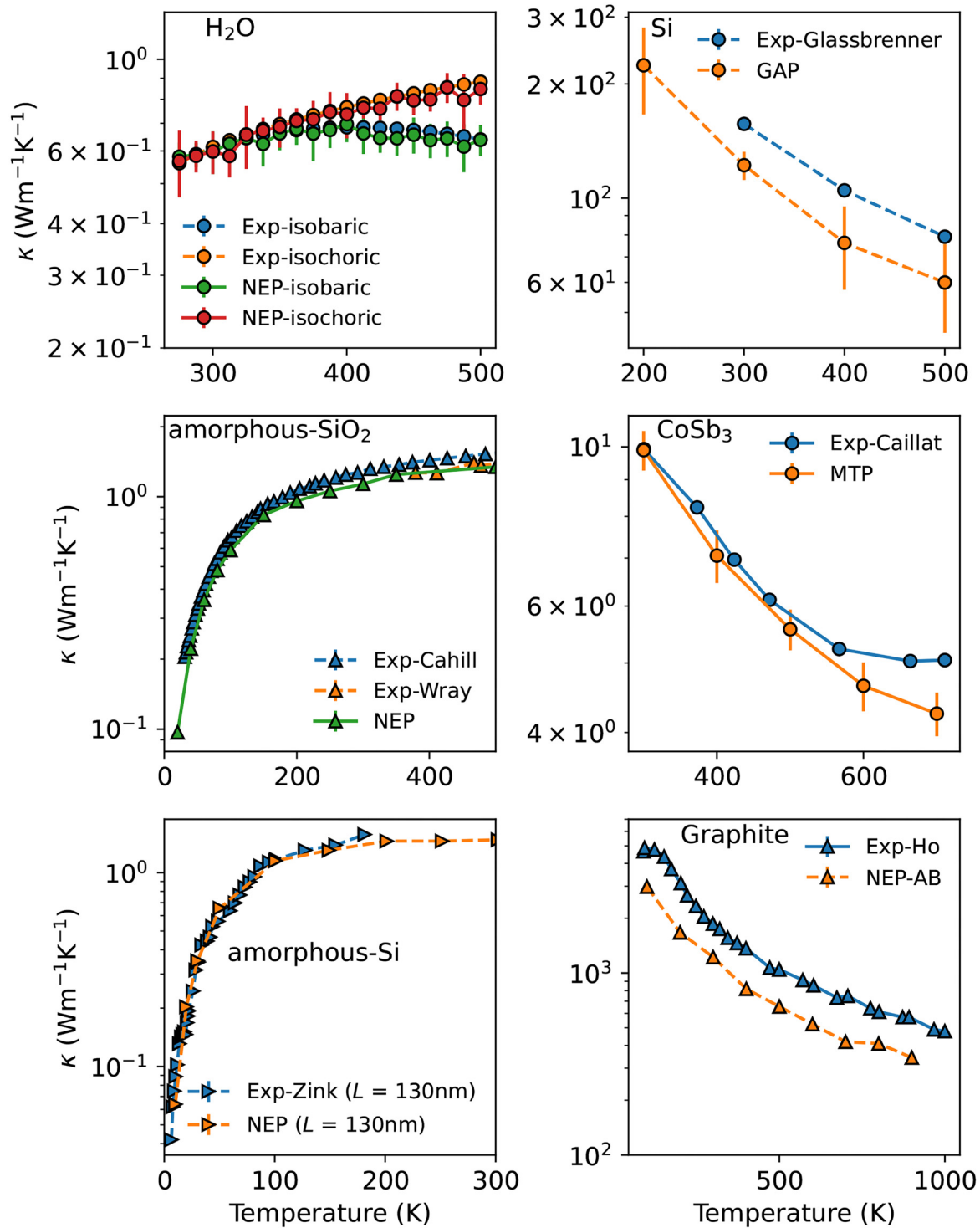


**FIG. 4.** Selected literature results on the application of MLPs to thermal transport, covering a broad range of materials, including liquid water,<sup>154</sup> amorphous SiO<sub>2</sub>,<sup>142</sup> amorphous silicon,<sup>152</sup> crystalline silicon,<sup>74</sup> crystalline CoSb<sub>3</sub>,<sup>78</sup> and crystalline graphite.<sup>141</sup> Experimental data are from Refs. 172 and 173 (liquid water), Refs. 174–176 (amorphous SiO<sub>2</sub>), Ref. 177 (amorphous silicon), Ref. 178 (crystalline silicon), Ref. 179 (crystalline CoSb<sub>3</sub>), and Ref. 180 (crystalline graphite).

27 April 2024 04:45:50

descriptor components are defined as ( $0 \leq n \leq n_{\max}^A$ ,  $1 \leq l \leq l_{\max}^{3\text{body}}$ )

$$q_{nl}^i = \sum_m (-1)^m A_{nlm}^i A_{nl(-m)}^i, \quad (43)$$

$$A_{nlm}^i = \sum_{j \neq i} g_n(r_{ij}) Y_{lm}(\hat{r}_{ij}). \quad (44)$$

Here,  $Y_{lm}$  are the spherical harmonics and  $\hat{r}_{ij}$  is the unit vector of  $\mathbf{r}_{ij}$ . Note that the radial functions  $g_n(r_{ij})$  for the radial and angular descriptor components can have different cutoff radii, which are denoted as  $r_c^R$  and  $r_c^A$ , respectively. For 4-body and 5-body descriptor components (with similar hyperparameters  $l_{\max}^{4\text{body}}$  and  $l_{\max}^{5\text{body}}$  as in the 3-body part), see Ref. 25.

### 3. The training algorithm

The free parameters are optimized using the SNES by minimizing a loss function that is a weighted sum of the root-mean-square errors (RMSEs) of energy, force, and virial stress, over  $N_{\text{gen}}$  generations with a population size of  $N_{\text{pop}}$ . The weights for the energy, force, and virial are denoted  $\lambda_e$ ,  $\lambda_f$ , and  $\lambda_v$ , respectively. Additionally, there are proper norm-1 ( $\ell_1$ ) and norm-2 ( $\ell_2$ ) regularization terms. For explicit details on the training algorithm, refer to Ref. 23.

### 4. Combining with other potentials

Although NEP with proper hyperparameters can account for almost all types of interactions, it can be useful to combine it with some well developed potentials, such as the Ziegler–Biersack–Littmark (ZBL)<sup>188</sup> potential for describing the extremely large screened nuclear repulsion at short interatomic distances and the D3 dispersion correction<sup>189</sup> for describing relatively long-range but weak interactions. Both potentials have been recently added to the GPUMD package.<sup>168,190</sup> It has been demonstrated that dispersion interactions can reduce the thermal conductivity of typical metal-organic frameworks by about 10%.<sup>168</sup> With the addition of ZBL and D3, NEP can then focus on describing the medium-range interactions.

## B. Model training and testing

There are educational articles focusing on various best practices in constructing MLPs.<sup>191,192</sup> Here, we use crystalline silicon as a specific example to illustrate the particular techniques in the context of NEP.

### 1. Prepare the initial training data

A training dataset is a collection of structures, each characterized by a set of attributes:

1. a cell matrix defining a periodic domain
2. the species of the atoms in the cell
3. the positions of the atoms
4. the total energy of the cell of atoms
5. the force vector acting on each of the atoms
6. (optionally) the total virial tensor (with six independent components) of the cell

The structures can be prepared by any method, while the energy, force, and virial are usually calculated via quantum mechanical methods, such as the DFT method. For a dataset comprising  $N_{\text{str}}$  structures with a total number of  $N$  atoms, there are  $N_{\text{str}}$  energy data,  $6N_{\text{str}}$  virial data, and  $3N$  force data.

While there are already several publicly available training datasets for silicon, we opt to create one from scratch for pedagogical purposes. The construction of training dataset typically involves an iterative process, employing a scheme similar to active learning. The iterative process begins with an initial dataset. To investigate heat transport in crystalline silicon, the initial training dataset should encompass structures relevant to the target temperatures and pressures. The most reliable way of generating structures under these conditions is through performing AIMD simulations, where interatomic forces are calculated based on quantum mechanical methods, such as the DFT approach. However, AIMD is computationally expensive (which is the primary motivation for developing a MLP) and it is often impractical to perform AIMD simulations for a dense grid of thermodynamic conditions. Fortunately, there is usually no such need for the purpose of generating the reference structures. Actually, manual perturbation of the atomic positions and/or the cell matrices proves to be an effective way of generating useful reference structures.

Based on the considerations above, we generate the initial training dataset through the following methods. First, we generate 50 structures by applying random strains (ranging from  $-3\%$  to  $+3\%$  for each degree of freedom) to the unit cell of cubic silicon (containing 8 atoms) while *simultaneously* perturbing the atomic positions randomly (by  $0.1 \text{ \AA}$ ). Second, we perform a 10-ps AIMD simulation at 1000 K (fixed cell) using a  $2 \times 2 \times 2$  supercell of silicon crystal containing 64 atoms, and sample the structures every 0.1 ps, obtaining another 100 structures. In total, we obtain 150 structures and 6800 atoms initially.

After obtaining the structures, we perform single-point DFT calculations to obtain the reference energy, force, and virial data. These data are saved to a file named `train.xyz`, using the extended XYZ format. The single-point DFT calculations are performed using the VASP package,<sup>193</sup> using the Perdew–Burke–Ernzerhof functional with the generalized gradient approximation,<sup>194</sup> a cutoff energy of 600 eV, an energy convergence threshold of  $10^{-6} \text{ eV}$ , and a  $k$ -point mesh of  $4 \times 4 \times 4$  for 64-atom supercells and  $12 \times 12 \times 12$  for 8-atom unit cells.

### 2. Train the first NEP model

With the training data, we proceed to train our first NEP model, denoted as NEP-iteration-1. For this task, we need to prepare an input file named `nep.in` for the `nep` executable in the GPUMD package. This `nep.in` input file contains the various hyperparameters for the NEP model under training. Most hyperparameters have well-suited default values, and for users initiating this process, it is recommended to use these defaults whenever applicable. The default values for key hyperparameters are as follows:

1.  $n_{\max}^R : 4$
2.  $n_{\max}^A : 4$

27 April 2024 04:45:50

- Chebyshev polynomial basis size for radial descriptor components  $N_{\text{bas}}^R : 12$
- Chebyshev polynomial basis size for angular descriptor components  $N_{\text{bas}}^A : 12$
- $l_{\text{max}}^{\text{body}} : 4$
- $r_{\text{max}}^{\text{body}} : 2$
- $l_{\text{max}}^{\text{body}} : 0$  (not used by default)
- $N_{\text{neu}} : 30$
- Energy and force weights  $\lambda_e$  and  $\lambda_f : 1$
- Virial weight  $\lambda_v : 0.1$
- Batch size: 1000 (a large or even full batch is preferred for training with SNES)
- Population size in SNES: 50
- Number of training generations (steps): 100 000
- ANN architecture: 30-30-1 (input layer 30, hidden layer 30, scalar output; relatively small but sufficient for most cases, expect for very complicated training data.)

Following this strategy, we use a very simple `nep.in` input file for our case, which is as follows:

```
type      1 Si
cutoff    5 5
```

In the first line, we specify the number of species (atom types) and the chemical symbol(s). In our example, there is only one species with the chemical symbol Si. In the second line, we specify the cutoff radii  $r_c^R$  and  $r_c^A$  for the  $g_n(r_{ij})$  functions in the radial and angular descriptor components, respectively. In our example, both cutoff radii are set to 5 Å, which includes the third nearest neighbors. The choice of cutoff radii is crucial for the performance of the trained NEP model and usually requires a systematic exploration to find an optimal set of values. It is important to note that the average number of neighbors, and hence the computational cost, scales cubically with respect to the cutoff radii. Therefore, blindly using large cutoff radii is not advisable. Although  $r_c^R = r_c^A$  in our current example, it is generally beneficial to use a larger  $r_c^R$  and a smaller  $r_c^A$ , because the radial descriptor components are computationally much cheaper than the angular descriptor components. Using a larger  $r_c^R$  does not lead to a significant increase in the computational cost, but can help capture longer-range interactions (such as screened Coulomb interactions in ionic compounds<sup>23</sup>) that typically have little angular dependence. A larger radial cutoff is also useful for capturing dispersion interactions in Van der Waals structures.<sup>141</sup>

The training results for NEP-iteration-1 are shown in Fig. 5(a). The RMSEs of force, energy, and virial all converge well within the default 100 000 training steps. The parity plots for force, energy, and virial in Figs. 5(b)–5(d) show good correlations between the NEP predictions and the DFT reference data. The RMSEs for energy, force, and virial are 1.0 meV/atom, 54.6 meV/Å, and 21.8 meV/atom, respectively.

### 3. Training iterations

Reliable assessment of the accuracy of a MLP typically involves an independent test dataset rather than the training dataset. To this end, we perform 10-ps MD simulations using NEP-iteration-1 in the *NPT* ensemble. The target pressure is set to zero, and the target temperatures range from 100 to 1000 K with intervals of 100 K. We sample 100 structures, totalling 6400 atoms.

We perform single-point DFT calculations for these structures and then use NEP-iteration-1 to generate predictions. This is achieved by adding the `prediction` keyword to the `nep.in` file:

```
type      1 Si
cutoff    5 5
prediction 1
```

This results in a rapid prediction for the test dataset. The RMSEs for energy, force, and virial are 1.2 meV/atom, 41.6 meV/Å, and 8.5 meV/atom, respectively. These values are already comparable to those for the training dataset, indicating that we can actually stop here and use NEP-iteration-1 as the final model. However, for added confidence, it is generally advisable to perform at least one more iteration. Therefore, we combine the test dataset (100 structures) with the training dataset (150 structures) to form an expanded training dataset (250 structures), and then train a new model named NEP-iteration-2. With this new NEP model, we generate another test dataset with 100 structures, using similar procedure as above but with a simulation time of 10 ns (instead of 10 ps), driven by NEP-iteration-2 for each temperature. The test RMSEs for NEP-iteration-2 are 0.5 meV/atom (energy), 33.5 meV/Å (force), and 8.9 meV/atom (virial), respectively. Both the energy and force RMSEs are smaller than those for the previous iteration, indicating the improved performance of NEP-iteration-2 compared to NEP-iteration-1.

The high accuracy of the latest test dataset sampled from 10-ns MD simulations driven by NEP-iteration-2 suggests that NEP-iteration-2 is a reliable model for MD simulation of crystalline silicon from 100 to 1000 K. Therefore, we conclude the iteration and use NEP-iteration-2 for the thermal transport applications. In the following, we will refer to NEP-iteration-2 simply as NEP. This NEP model, running on a consumer-grade NVIDIA RTX 4090 GPU card with 24 GB of memory, achieves a remarkable computational speed of about  $2.4 \times 10^7$  atom-step/second, equivalent to a computational cost of about  $4.2 \times 10^{-8}$  s/atom/step in MD simulations.

Using a trained MLP to generate MD trajectory is a common practice in nearly all the active-learning schemes documented in the literature. The major difference between different active-learning schemes is about the criteria for selecting structures to be added to the training dataset. While there might be a risk of sampling nonphysical structures using a trained MLP model, as demonstrated in this tutorial, one can mitigate the risk by conducting a few iterations and employing shorter MD runs in the initial stages, progressively increasing the MD simulation time with each iteration. As a result, the MLP becomes increasingly reliable throughout

27 April 2024 04:45:50

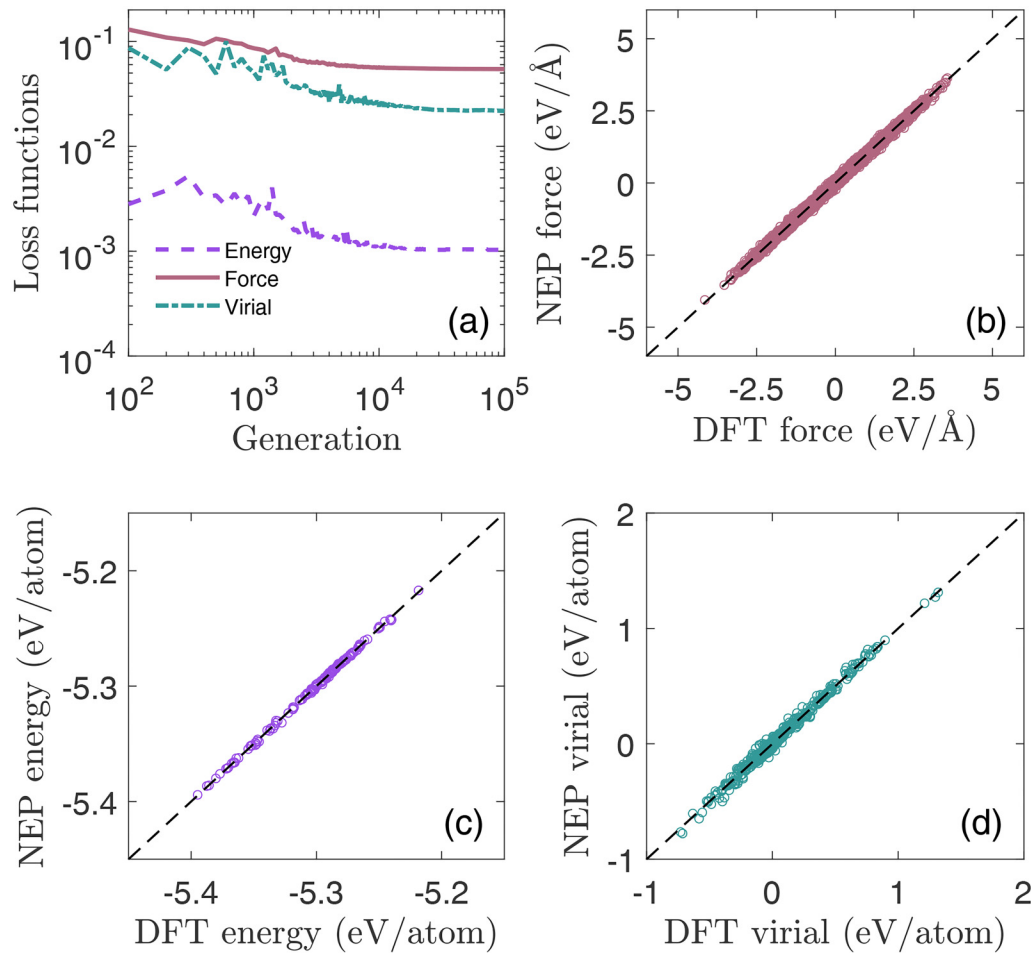


**FIG. 5.** (a) Evolution of RMSEs of energy, force, and virial with respect to training generations (steps). (b) Comparison of force, (c) energy, and (d) virial calculated by NEP against DFT reference data for the initial training dataset.

the iteration process, enabling the generation of longer and more accurate trajectories over time. In our example using the silicon crystal, a relatively simple system, we only performed two iterations to achieve accurate predictions for 10-ns MD runs. However, for more complex systems, one might need to perform more iterations, increasing the MD steps more gradually than what we have demonstrated for the silicon crystal example.

## C. Thermal transport applications

### 1. Phonon dispersion relations

Before applying a MLP to thermal transport applications, it is usually a good practice to examine the phonon dispersion relations. The phonon dispersion relations for NEP and Tersoff<sup>195</sup> potentials are calculated using GPUMD, employing the finite-displacement method with a displacement of 0.01 Å. For DFT, we use density functional perturbation theory as implemented in VASP in

combination with PHONOPY,<sup>196</sup> using a  $4 \times 4 \times 4$  supercell, a cutoff energy of 600 eV, an energy convergence threshold of  $10^{-8}$  eV, and a  $5 \times 5 \times 5$   $k$ -point mesh.

In Fig. 6, we compare the phonon dispersion relations calculated from DFT, Tersoff potential, and NEP. While there are small differences between NEP and DFT results, the agreement between NEP and DFT is significantly better than that between Tersoff and DFT. The agreement between NEP and DFT can, in principle, be further improved, for example, by increasing the size of the ANN model and/or the cutoff radii. However, this comes with a trade-off, as it may reduce computational efficiency. In practice, achieving a balance between accuracy and speed is essential.

### 2. Thermal conductivity from EMD

After validating the phonon dispersion relations, we proceed to thermal conductivity calculations using the various MD



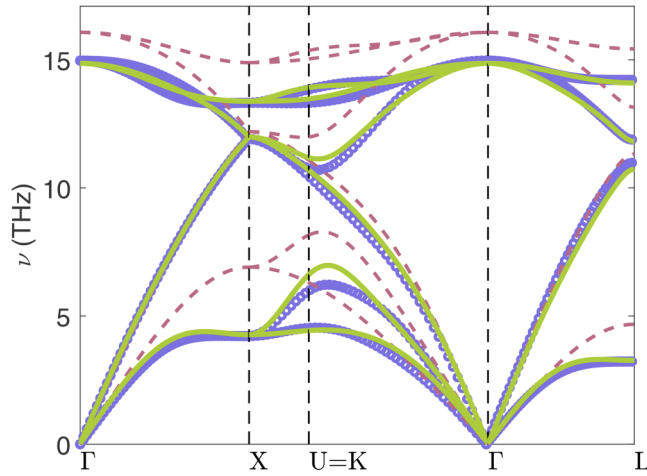


**FIG. 6.** Phonon dispersion relations of silicon from DFT (circles), Tersoff potential (dashed lines), and NEP (solid lines).

methods, as reviewed in Sec. III. All calculations are performed using the `gpumd` executable in `GPUMD`.

We start with the EMD method, using a sufficiently large  $12 \times 12 \times 12$  cubic supercell with 13 824 atoms. The `run.in` file for the `gpumd` executable is configured as follows:

```
potential      nep.txt
velocity      300

ensemble      npt_ber 300 300 100 0 53.4059 2000
time_step     1
dump_thermo   1000
run           500000

ensemble      nve
compute_hac   20 50000 10
run           10000000
```

There are three input blocks. In the first block, we specify the NEP potential file and set the initial temperature to 300 K. The second block represents an equilibration run of 500 ps in the *NPT* ensemble, aiming to reach a target temperature of 300 K and a target pressure of zero. The third block corresponds to a production run of 10 ns in the *NVE* ensemble, with heat current sampled every 20 steps.

We perform 50 independent runs using the inputs above, each with a different set of initial velocities. The  $\kappa(t)$  [cf. Eq. (26)] results from individual runs (thin solid lines) and their average (thick solid line) and error bounds (thick dashed lines) are shown in Fig. 7(a). Taking  $t = 1$  ns as the upper limit of the correlation time, up to which  $\kappa(t)$  converges well, we have  $\kappa \approx 102 \pm 6 \text{ W m}^{-1} \text{ K}^{-1}$  from the EMD method. In this work, all statistical errors are calculated as the standard error of the mean.

### 3. Thermal conductivity from HNEMD

We then move to the HNEMD method. Since the HNEMD method has the same finite-size effects as in the EMD method, we use the same simulation cell as in the EMD method. The `run.in` file for the `gpumd` executable reads as follows:

```
potential      nep.txt
velocity      300

ensemble      npt_ber 300 300 100 0 53.4059 2000
time_step     1
dump_thermo   1000
run           1000000

ensemble      nvt_nhc 300 300 100
compute_hnemd 1000 2e-5 0 0
compute_shc   2 250 0 1000 120
dump_thermo   1000
run           10000000
```

There are also three input blocks, and only the production block differs from the case of EMD. Here, the temperature is controlled using the Nosé–Hoover chain thermostat, and an external force in the  $x$  direction with  $F_e = 2 \times 10^{-5} \text{ Å}^{-1}$  is applied. The production run has 10 ns in total.

We perform 4 independent runs using the specified inputs, each with a different set of initial velocities. The  $\kappa(t)$  [cf. Eq. (34)] results from individual runs (thin solid lines) and their average (thick solid line) and error bounds (thick dashed lines) are shown in Fig. 7(b). The estimated thermal conductivity is  $\kappa \approx 108 \pm 4 \text{ W m}^{-1} \text{ K}^{-1}$ , consistent with the EMD value within statistical error bounds. It is noteworthy that the total production time for the HNEMD simulations ( $4 \times 10$  ns) is considerably smaller than that for the EMD simulations ( $50 \times 10$  ns), while the former still gives a smaller statistical error. This suggests a higher computational efficiency of the HNEMD over the EMD method, as previously emphasized.<sup>54</sup>

From the HNEMD simulations, we also obtain the spectral thermal conductivity  $\kappa(\omega)$  [cf. Eq. (39)]. By combining this with the spectral conductance  $G(\omega)$  [cf. Eq. (37)] in a ballistic NEMD simulation (details provided below), we calculate the phonon MFP spectrum as

$$\lambda(\omega) = \frac{\kappa(\omega)}{G(\omega)}, \quad (45)$$

which is a generalization of Eq. (8). The calculated  $\lambda(\omega)$  is shown in Fig. 7(c). Remarkably, in the low-frequency limit,  $\lambda(\omega)$  can go well beyond one micron. With  $\kappa(\omega)$  and  $\lambda(\omega)$ , one can calculate the spectral apparent thermal conductivity  $\kappa(\omega, L)$  according to Eq. (10) and obtain the apparent thermal conductivity at *any* length  $L$  using Eq. (11). The results are depicted by the solid line in Fig. 7(d).

27 April 2024 04:45:50



#### 4. Thermal conductivity from NEMD

The third MD method we demonstrate is the NEMD method, using the fixed boundary setup discussed in Sec. II C 2. We explore lengths  $L = 2.7, 5.5, 11.0, 21.9, 43.8, 87.6, 175.3, 350.5$  nm, maintaining a consistent  $5 \times 5$  cell in the transverse direction. The heat source and sink regions span 4.4 nm, which is long enough to ensure fully thermalized phonons within these regions. The `run.in` input file for our NEMD simulations reads as follows:

```
potential      nep.txt
velocity      300

ensemble      nvt_ber 300 300 100
time_step     1
fix           0
dump_thermo   100
run           100000

ensemble      heat_lan 300 100 10 1 7
fix           0
compute       0 10 100 temperature
compute_shc   2 250 0 1000 120.0 group 0 4
run           2000000
```

Unlike the EMD and HNEMD simulations, the NEMD simulations involve an extra operation: certain atoms are frozen. We assign these atoms to the “group” 0 and use the `fix 0` command to freeze them. In the production stage, two Langevin thermostats with different temperatures are applied separately to groups 1 and 7, corresponding to the heat source and the heat sink, respectively. The temperature difference between them is set to 20 K. The heat flux can be obtained from the data produced by the `compute` keyword, allowing us to calculate the apparent thermal conductivity  $\kappa(L)$  according to Eq. (29). The production stage has a duration of 2 ns, with a well-established steady state achieved within the first 1 ns. Therefore, we use the second half of the production time to calculate the aforementioned steady-state properties. For each system length, we perform 2 independent runs, each with a different set of initial velocities. To get the spectral conductance  $G(\omega)$  in the ballistic limit, as used in Eq. (45), we use the data produced by the `compute_shc` keyword in NEMD simulations with a short system length of  $L = 1.6$  nm.

As expected, the  $\kappa(L)$  values from NEMD simulations match well with the  $\kappa(L)$  curve from the HNEMD-based formalism [Fig. 7(d)]. However, reaching the diffusive limit directly through NEMD simulations is computationally demanding. Considering the presence of different phonon MFPs [Fig. 7(c)] in the system, linear extrapolation to the diffusive limit based on a limited number of  $\kappa(L)$  values from NEMD simulations is often inadequate. This limitation arises because the relation between  $1/\kappa(L)$  and  $1/L$  becomes nonlinear in the large- $L$  limit (see Fig. 8). This nonlinearity is a general feature in realistic materials, as also demonstrated in our toy model [Fig. 2(d)].

As of now, we have demonstrated the full consistency among the three MD-based methods. Notably, the HNEMD method stands out as the most computationally efficient. This explains why most works based on `GPUMD` utilize the HNEMD method, with the other two methods typically being employed primarily for sanity-checking the results.

#### 5. Comparison with experiments

After obtaining consistent results from three MD methods, we are ready to compare the results with experimental data. The thermal conductivity of crystalline silicon is measured to be about  $150 \text{ W m}^{-1} \text{ K}^{-1}$ , but our HNEMD simulations predict a value of  $108 \pm 4 \text{ W m}^{-1} \text{ K}^{-1}$ , which is only 72% of the experimental value. As a comparison, the thermal conductivity of crystalline silicon has been calculated<sup>197</sup> to be about  $250 \pm 10 \text{ W m}^{-1} \text{ K}^{-1}$  using a Tersoff potential,<sup>195</sup> which is 167% of the experimental value. Specifically, the Tersoff potential appears to underestimate the phonon anharmonicity, while the NEP model tends to overestimate it.

According to a recent unpublished study by Wu *et al.*,<sup>181</sup> the underestimation of thermal conductivity by MLPs could potentially be attributed to small but finite force errors compared to the reference data, leading to extra phonon scatterings. Based on the fact that the force errors form a Gaussian distribution, similar to the random forces in the Langevin thermostat, a method for correcting the force-error-induced underestimation of the thermal conductivity from MLPs is proposed.<sup>181</sup> This correction involves conducting a series of HNEMD simulations with the temperature being controlled by a Langevin thermostat with various relaxation times  $\tau_T$ . Each component of the random force follows a Gaussian distribution with zero mean and a variance of

$$\sigma_{\text{lan}}^2 = \frac{2k_B T m}{\tau_T \Delta t}, \quad (46)$$

where  $m$  is the average atom mass in the system and  $\Delta t$  is the integration time step. When the random forces in the Langevin thermostat and the force errors in the MLP (with a RMSE of  $\sigma_{\text{mlp}}$  at a particular temperature) are present simultaneously, a new set of force errors is created, with a larger variance given by

$$\sigma_{\text{tot}}^2 = \sigma_{\text{lan}}^2 + \sigma_{\text{mlp}}^2, \quad (47)$$

according to the properties of Gaussian distribution. After obtaining  $\kappa(\sigma_{\text{tot}})$  at different  $\sigma_{\text{tot}}$ , the thermal conductivity with zero total force error  $\kappa(\sigma_{\text{tot}} = 0)$  can be obtained from the following relation:<sup>181</sup>

$$\frac{1}{\kappa(\sigma_{\text{tot}})} = \frac{1}{\kappa(\sigma_{\text{tot}} = 0)} + \beta \sigma_{\text{tot}}, \quad (48)$$

where  $\beta$  is a fitting parameter.

Based on the correction method, we perform HNEMD simulations using the Langevin thermostat with the following set of  $\tau_T$  values: 30, 50, 100, 200, and 500 ps. From these, the  $\sigma_L$  values are calculated to be 17.3, 27.4, 38.7, 54.8, and 70.7 meV/Å. At 300 K, the force RMSE for our NEP model is tested to be  $\sigma_{\text{mlp}} = 21.2$  meV/Å. Therefore, the resulting  $\sigma_{\text{tot}}$  values are 27.4, 34.6, 44.2, 58.7, and 73.8 meV/Å. To ensure consistency with experimental conditions, we

27 April 2024 04:45:50

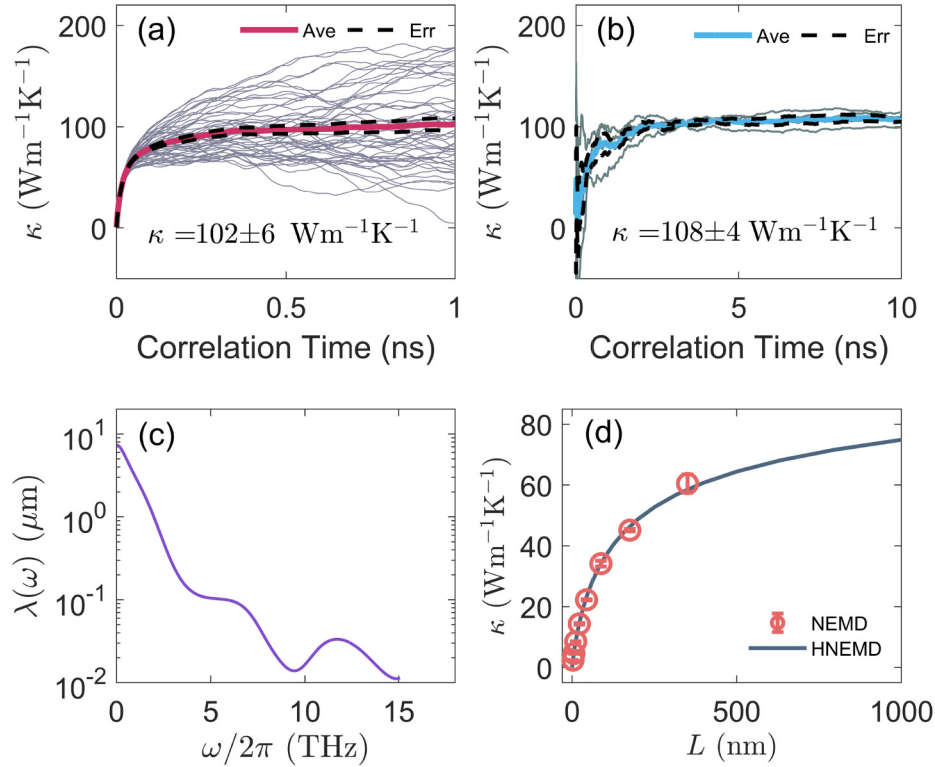


**FIG. 7.** Thermal conductivity of crystalline silicon at 300 K from three MD-based methods using the herein developed NEP. (a) Results from 50 independent EMD runs (thin solid lines), along with their average (thick solid line) and error bounds (thick dashed lines); (b) Results from four independent HNEMD runs (thin solid lines), along with their average (thick solid line) and error bounds (thick dashed lines); (c) Phonon MFP spectrum calculated using spectral decomposition method; (d) Results from NEMD simulations (red symbols), matching the  $\kappa(L)$  curve from the HNEMD-based formalism.

27 April 2024 04:45:50

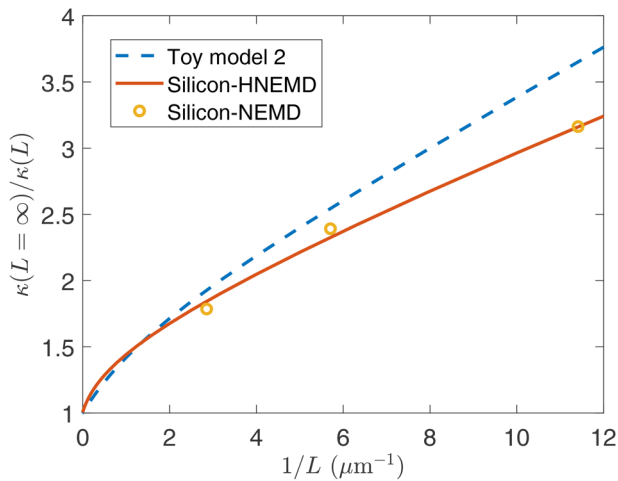


**FIG. 8.** The nonlinearity in the relation between  $\kappa(L = \infty)/\kappa(L)$  and  $1/L$  in the large- $L$  limit, observed in the second toy model [as discussed in Fig. 2(d)] and the silicon example.

also account for the presence of a few Si isotopes (92.2%  $^{28}\text{Si}$ , 4.7%  $^{29}\text{Si}$ , and 3.1%  $^{30}\text{Si}$ ) in the calculations. The calculated  $\kappa(\sigma_{\text{tot}})$  with the various  $\sigma_{\text{tot}}$  are shown in Fig. 9(a). By fitting these data, we obtain a corrected thermal conductivity of  $\kappa(\sigma_{\text{tot}} = 0) = 145 \text{ W m}^{-1} \text{ K}^{-1}$ , in excellent agreement with the experimental value.

The extrapolation scheme described by Eq. (48) not only applies to a single NEP model with different levels of intentionally added random forces through the Langevin thermostat, but is also valid for different NEP models with varying accuracy. To demonstrate this, we construct two extra NEP models with reduced accuracy. Starting from the default hyperparameters, we construct the first extra NEP model by reducing the number of neurons in the hidden layer from 30 to 1, resulting in an increased force RMSE of 32.4 meV/Å. Based on this, we then construct the second extra NEP model by further reducing the Chebyshev polynomial basis sizes ( $N_{\text{bas}}^R$ ,  $N_{\text{bas}}^A$ ) from (12, 12) to (4, 4), resulting in a further increased force RMSE of 52.9 meV/Å. The thermal conductivity results from the three NEP models with different accuracy using the Nosé–Hoover chain thermostat also closely follow the extrapolation curve [Fig. 9(a)], providing further support for the validity of the extrapolation scheme Eq. (48).

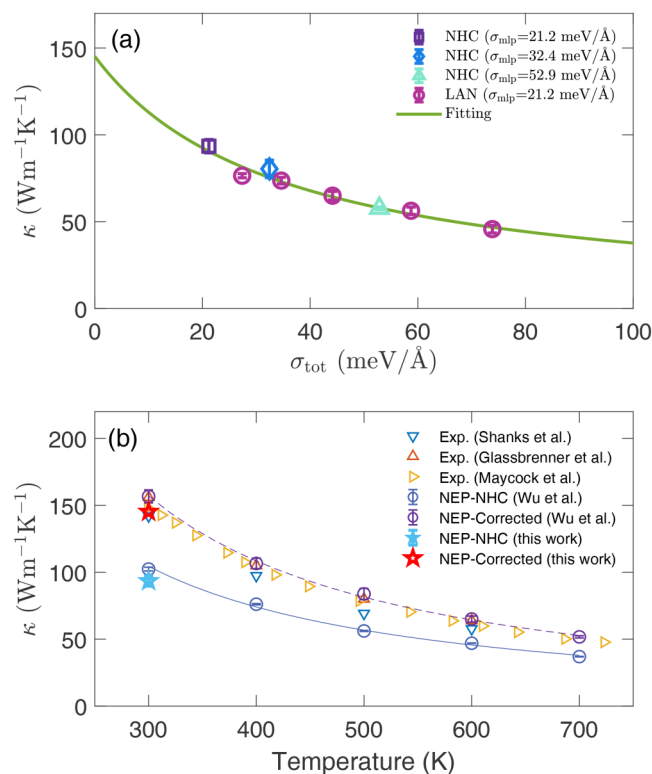


**FIG. 9.** (a) Thermal conductivity of crystalline silicon at 300 K from HNEMD simulations using the herein developed NEP models as a function of the total force error  $\sigma_{\text{tot}}$ . NHC and LAN represent the Nosé–Hoover chain and Langevin thermostating methods, respectively. The data are fitted to obtain the corrected thermal conductivity of  $\kappa(\sigma_{\text{tot}} = 0) = 145 \text{ W m}^{-1} \text{ K}^{-1}$ . (b) Comparison of simulation results before and after the correction with experimental values<sup>178,198,199</sup> and previously (uncorrected and corrected) NEP-MD simulations.<sup>181</sup>

Our results for 300 K before and after the correction are consistent with those reported in the previous work,<sup>181</sup> which also uses a NEP model [Fig. 9(b)]. In Fig. 9(b), we also show the results for other temperatures<sup>181</sup> in comparison to the experimental data. The corrected results agree well with the experimental ones across a broad range of temperatures. The slightly higher values from corrected NEP model predictions are likely due to the fact that isotope disorder was not considered in the previous calculations.<sup>181</sup>

While we have only demonstrated the application of the extrapolation (correction) method to HNEMD simulations, it is worth noting that this method is also potentially applicable to EMD simulations. We speculate that the force errors in MLPs may also play a role in ALD-based approaches for thermal transport.

## V. SUMMARY AND CONCLUSIONS

In summary, we have provided a comprehensive pedagogical introduction to MD simulations of thermal transport utilizing the NEP MLP as implemented in the GPUMD package.

We began by reviewing fundamental concepts related to thermal transport in both ballistic and diffusive regimes, elucidating the explicit expression of the heat flux in the context of MLPs, and exploring various MD-based methods for thermal transport studies, including EMD, NEMD, HNEMD, and spectral decomposition.

Following this, we conducted an up-to-date review of the literature on the application of MLPs in thermal transport problems through MD simulations.

A detailed review of the NEP approach followed, with a step-by-step demonstration of the process of developing an accurate and efficient NEP model for crystalline silicon applicable across a range of temperatures. Utilizing the developed NEP model, we explained the technical details of all MD-based methods for thermal transport discussed in this work. Finally, we compared the simulation results with experimental data, addressing the common trend of thermal conductivity underestimation by MLPs and demonstrating an effective correction method.

By completing this tutorial, readers will be equipped to construct MLPs and seamlessly integrate them into highly efficient and predictive MD simulations of heat transport.

## ACKNOWLEDGMENTS

H.D. is supported by the Science Foundation from the Education Department of Liaoning Province (No. JYTMS20231613) and the Doctoral start-up Fund of Bohai University (No. 0523bs008). P.Y. is supported by the Israel Academy of Sciences and Humanities & Council for Higher Education Excellence Fellowship Program for International Postdoctoral Researchers. K.X. and T.L. acknowledge support from the National Key R&D Project from Ministry of Science and Technology of China (No. 2022YFA1203100), the Research Grants Council of Hong Kong (No. AoE/P-701/20), and RGC GRF (No. 14220022). Z.Z. acknowledges the European Union's Horizon 2020 research and innovation programme under the Marie Skłodowska-Curie Grant Agreement No. 101034413. S.X. acknowledges financial support from the National Natural Science Foundation of China (NNSFC) (Grant No. 12174276).

## AUTHOR DECLARATIONS

### Conflict of Interest

The authors have no conflicts to disclose.

### Author Contributions

**Haikuan Dong:** Conceptualization (equal); Data curation (equal); Formal analysis (equal); Investigation (equal); Methodology (equal); Resources (equal); Software (equal); Validation (equal); Visualization (equal); Writing – original draft (equal). **Yongbo Shi:** Conceptualization (equal); Data curation (equal); Formal analysis (equal); Investigation (equal); Methodology (equal); Validation (equal); Visualization (equal); Writing – original draft (equal). **Penghua Ying:** Conceptualization (equal); Data curation (equal); Formal analysis (equal); Investigation (equal); Methodology (equal); Software (equal); Validation (equal); Visualization (equal); Writing – original draft (equal); Writing – review & editing (equal). **Ke Xu:** Conceptualization (equal); Data curation (equal);

27 April 2024 04:45:50

Formal analysis (equal); Investigation (equal); Methodology (equal); Software (equal); Validation (equal); Visualization (equal); Writing – original draft (equal). **Ting Liang:** Conceptualization (equal); Formal analysis (equal); Investigation (equal); Methodology (equal); Software (equal); Validation (equal); Writing – review & editing (equal). **Yanzhou Wang:** Conceptualization (equal); Data curation (equal); Formal analysis (equal); Investigation (equal); Methodology (equal); Software (equal); Visualization (equal); Writing – original draft (equal); Writing – review & editing (equal). **Zezhu Zeng:** Conceptualization (equal); Formal analysis (equal); Investigation (equal); Methodology (equal); Software (equal); Validation (equal); Writing – original draft (equal). **Xin Wu:** Conceptualization (equal); Investigation (equal); Methodology (equal); Validation (equal); Writing – review & editing (equal). **Wenjiang Zhou:** Conceptualization (equal); Data curation (equal); Formal analysis (equal); Investigation (equal); Methodology (equal); Validation (equal); Writing – original draft (equal). **Shiyun Xiong:** Conceptualization (equal); Investigation (equal); Methodology (equal); Validation (equal); Writing – review & editing (equal). **Shunda Chen:** Conceptualization (equal); Formal analysis (equal); Investigation (equal); Methodology (equal); Validation (equal); Visualization (equal); Writing – original draft (equal); Writing – review & editing (equal). **Zheyong Fan:** Conceptualization (equal); Data curation (equal); Formal analysis (equal); Investigation (equal); Methodology (equal); Software (equal); Validation (equal); Visualization (equal); Writing – original draft (equal); Writing – review & editing (equal).

## DATA AVAILABILITY

All the training and test datasets and the trained NEP models for crystalline silicon are freely available at <https://gitlab.com/brucefan1983/nep-data>. The training datasets, trained NEP, DP, and MTP models for graphene and MD input files for reproducing Fig. 3 are freely available at [https://github.com/hityingph/supporting-info/tree/main/Dong\\_GPUMD\\_Tutorial\\_2024](https://github.com/hityingph/supporting-info/tree/main/Dong_GPUMD_Tutorial_2024).

## APPENDIX: DETAILS ON HEAT CURRENT VALIDATION

To validate the implementation of heat current for NEP, DP, and MTP (see Fig. 3), we use a common reference dataset to train a model for each of the three MLPs. We take all the monolayer graphene structures from Ref. 67 and use 3288 structures (99 493 atoms) as our training dataset and 822 structures (25 035 atoms) as our test dataset, respectively.

For NEP, we set  $r_c^R = 6 \text{ \AA}$ ,  $r_c^A = 4 \text{ \AA}$ ,  $N_{\text{neu}} = 50$ ,  $N_{\text{gen}} = 5 \times 10^5$ , while keeping other hyperparameters as the defaults. For DP, the DEEPM-DKIT package (version 2.1.4)<sup>21</sup> is used, with the `se_a` descriptor with a cutoff radius of 6 Å. The dimensions of the embedding network are set to (25, 50, 100), and the fitting network dimensions are configured as (240, 240, 240). Initially, the weighting parameters for energy and forces are set to 0.02 and 1000, respectively, and are linearly adjusted to 1 for both during the training process. The training comprises  $4 \times 10^6$  steps, with a learning rate that is exponentially decreased from  $10^{-3}$  to  $10^{-8}$ . For MTP, the `MLIP` (version 2) package<sup>20</sup> is used. The descriptor “level” for MTP is set to 18, with a cutoff radius of 6 Å.

**TABLE III.** Comparison of the energy and force RMSEs and computational speed for MTP, DP (after model compression), and NEP. The computational speed is assessed by running MD simulations for  $10^5$  steps in the NV7 ensemble for a graphene system containing 24 800 atoms, using GPUMD (NEP) or LAMMPS<sup>32</sup> with version 23 Jun 2022 (MTP and DP). For GPU-based tests (DP and NEP), a single Nvidia RTX 3090 is used; for CPU-based tests (MTP), 64 AMD EPYC 7H12 cores are used.

Model	MTP	DP	NEP
Energy-train (meV/atom)	2.4	1.4	1.8
Energy-test (meV/atom)	2.2	1.4	1.9
Force-train (meV/Å)	119	75	91
Force-test (meV/Å)	116	78	89
Speed ( $10^5$ atom-step/s)	3.9	1.8	100

Table III presents the performance metrics for the three MLP models.

We then conduct NEMD simulations to validate the implementations of heat current in the three MLPs by checking the consistency between the accumulated heat in atoms within the transport region [cf. Eq. (25)] and that obtained from the thermostats [cf. Eq. (31)]. The NEMD simulation procedure is similar to that as described in Sec. IV C 4 for silicon. The transport is set to be along the armchair direction of a graphene sample with a width of 2.5 nm and a length of 426 nm (excluding the thermostatted regions). The data presented in Fig. 3 are sampled during the last 1.5 ns of the NEMD simulations, during which a steady state is achieved.

## REFERENCES

- <sup>1</sup>S. Volz, J. Ordóñez-Miranda, A. Shchepetov, M. Prunnila, J. Ahopelto, T. Pezeril, G. Vaudel, V. Gusev, P. Ruello, E. M. Weig, M. Schubert, M. Hettich, M. Grossman, T. Dekorsy, F. Alzina, B. Graczykowski, E. Chavez-Angel, J. Sebastian Reparaz, M. R. Wagner, C. M. Sotomayor-Torres, S. Xiong, S. Neogi, and D. Donadio, “Nanophononics: State of the art and perspectives,” *Eur. Phys. J. B* **89**, 15 (2016).
- <sup>2</sup>N. Li, J. Ren, L. Wang, G. Zhang, P. Hänggi, and B. Li, “Colloquium: Phononics: Manipulating heat flow with electronic analogs and beyond,” *Rev. Mod. Phys.* **84**, 1045–1066 (2012).
- <sup>3</sup>X. Gu, Z. Fan, and H. Bao, “Thermal conductivity prediction by atomistic simulation methods: Recent advances and detailed comparison,” *J. Appl. Phys.* **130**, 210902 (2021).
- <sup>4</sup>L. Isaeva, G. Barbalinardo, D. Donadio, and S. Baroni, “Modeling heat transport in crystals and glasses from a unified lattice-dynamical approach,” *Nat. Commun.* **10**, 3853 (2019).
- <sup>5</sup>M. Simoncelli, N. Marzari, and F. Mauri, “Unified theory of thermal transport in crystals and glasses,” *Nat. Phys.* **15**, 809–813 (2019).
- <sup>6</sup>M. Simoncelli, N. Marzari, and F. Mauri, “Wigner formulation of thermal transport in solids,” *Phys. Rev. X* **12**, 041011 (2022).
- <sup>7</sup>Z.-Y. Ong, “Tutorial: Concepts and numerical techniques for modeling individual phonon transmission at interfaces,” *J. Appl. Phys.* **124**, 151101 (2018).
- <sup>8</sup>A. J. H. McGaughey, A. Jain, H.-Y. Kim, and B. Fu, “Phonon properties and thermal conductivity from first principles, lattice dynamics, and the Boltzmann transport equation,” *J. Appl. Phys.* **125**, 011101 (2019).
- <sup>9</sup>Z. Liang and M. Hu, “Tutorial: Determination of thermal boundary resistance by molecular dynamics simulations,” *J. Appl. Phys.* **123**, 191101 (2018).
- <sup>10</sup>J. Chen, X. Xu, J. Zhou, and B. Li, “Interfacial thermal resistance: Past, present, and future,” *Rev. Mod. Phys.* **94**, 025002 (2022).



- <sup>11</sup>A. Marcolongo, P. Umari, and S. Baroni, "Microscopic theory and quantum simulation of atomic heat transport," *Nat. Phys.* **12**, 80–84 (2016).
- <sup>12</sup>C. Carbogno, R. Ramprasad, and M. Scheffler, "Ab initio Green–Kubo approach for the thermal conductivity of solids," *Phys. Rev. Lett.* **118**, 175901 (2017).
- <sup>13</sup>J. Kang and L.-W. Wang, "First-principles Green–Kubo method for thermal conductivity calculations," *Phys. Rev. B* **96**, 020302 (2017).
- <sup>14</sup>F. Knoop, M. Scheffler, and C. Carbogno, "Ab initio Green–Kubo simulations of heat transport in solids: Method and implementation," *Phys. Rev. B* **107**, 224304 (2023).
- <sup>15</sup>J. Behler and M. Parrinello, "Generalized neural-network representation of high-dimensional potential-energy surfaces," *Phys. Rev. Lett.* **98**, 146401 (2007).
- <sup>16</sup>A. P. Bartók, M. C. Payne, R. Kondor, and G. Csányi, "Gaussian approximation potentials: The accuracy of quantum mechanics, without the electrons," *Phys. Rev. Lett.* **104**, 136403 (2010).
- <sup>17</sup>M. A. Caro, "Optimizing many-body atomic descriptors for enhanced computational performance of machine learning based interatomic potentials," *Phys. Rev. B* **100**, 024112 (2019).
- <sup>18</sup>J. Byggmästar, K. Nordlund, and F. Djurabekova, "Simple machine-learned interatomic potentials for complex alloys," *Phys. Rev. Mater.* **6**, 083801 (2022).
- <sup>19</sup>A. Thompson, L. Swiler, C. Trott, S. Foiles, and G. Tucker, "Spectral neighbor analysis method for automated generation of quantum-accurate interatomic potentials," *J. Comput. Phys.* **285**, 316–330 (2015).
- <sup>20</sup>I. S. Novikov, K. Gubaev, E. V. Podryabinkin, and A. V. Shapeev, "The MLIP package: Moment tensor potentials with MPI and active learning," *Mach. Learn.: Sci. Technol.* **2**, 025002 (2020).
- <sup>21</sup>H. Wang, L. Zhang, J. Han, and E. Weinan, "Deepmd-kit: A deep learning package for many-body potential energy representation and molecular dynamics," *Comput. Phys. Commun.* **228**, 178–184 (2018).
- <sup>22</sup>R. Drautz, "Atomic cluster expansion for accurate and transferable interatomic potentials," *Phys. Rev. B* **99**, 014104 (2019).
- <sup>23</sup>Z. Fan, Z. Zeng, C. Zhang, Y. Wang, K. Song, H. Dong, Y. Chen, and T. Ala-Nissila, "Neuroevolution machine learning potentials: Combining high accuracy and low cost in atomistic simulations and application to heat transport," *Phys. Rev. B* **104**, 104309 (2021).
- <sup>24</sup>Z. Fan, "Improving the accuracy of the neuroevolution machine learning potential for multi-component systems," *J. Phys.: Condens. Matter* **34**, 125902 (2022).
- <sup>25</sup>Z. Fan, Y. Wang, P. Ying, K. Song, J. Wang, Y. Wang, Z. Zeng, K. Xu, E. Lindgren, J. M. Rahm, A. J. Gabourie, J. Liu, H. Dong, J. Wu, Y. Chen, Z. Zhong, J. Sun, P. Erhart, Y. Su, and T. Ala-Nissila, "GPUMD: A package for constructing accurate machine-learned potentials and performing highly efficient atomistic simulations," *J. Chem. Phys.* **157**, 114801 (2022).
- <sup>26</sup>Z. Fan, W. Chen, V. Vierimaa, and A. Harju, "Efficient molecular dynamics simulations with many-body potentials on graphics processing units," *Comput. Phys. Commun.* **218**, 10–16 (2017).
- <sup>27</sup>K. Song, R. Zhao, J. Liu, Y. Wang, E. Lindgren, Y. Wang, S. Chen, K. Xu, T. Liang, P. Ying, N. Xu, Z. Zhao, J. Shi, J. Wang, S. Lyu, Z. Zeng, S. Liang, H. Dong, L. Sun, Y. Chen, Z. Zhang, W. Guo, P. Qian, J. Sun, P. Erhart, T. Ala-Nissila, Y. Su, and Z. Fan, "General-purpose machine-learned potential for 16 elemental metals and their alloys" (2023), [arXiv:2311.04732](https://arxiv.org/abs/2311.04732) [cond-mat.mtrl-sci].
- <sup>28</sup>J. F. Nye, *Physical Properties of Crystals: Their Representation by Tensors and Matrices* (Oxford University Press, 1985).
- <sup>29</sup>S. Datta, *Electronic Transport in Mesoscopic Systems* (Cambridge University Press, 1995).
- <sup>30</sup>D. A. McQuarrie, *Statistical Mechanics* (University Science Books, 2000).
- <sup>31</sup>Z. Fan, L. F. C. Pereira, H.-Q. Wang, J.-C. Zheng, D. Donadio, and A. Harju, "Force and heat current formulas for many-body potentials in molecular dynamics simulations with applications to thermal conductivity calculations," *Phys. Rev. B* **92**, 094301 (2015).
- <sup>32</sup>A. P. Thompson, H. M. Aktulga, R. Berger, D. S. Bolintineanu, W. M. Brown, P. S. Crozier, P. J. in 't Veld, A. Kohlmeyer, S. G. Moore, T. D. Nguyen, R. Shan, M. J. Stevens, J. Tranchida, C. Trott, and S. J. Plimpton, "LAMMPS—A flexible simulation tool for particle-based materials modeling at the atomic, meso, and continuum scales," *Comput. Phys. Commun.* **271**, 108171 (2022).
- <sup>33</sup>P. Boone, H. Babaei, and C. E. Wilmer, "Heat flux for many-body interactions: Corrections to LAMMPS," *J. Chem. Theory Comput.* **15**, 5579–5587 (2019).
- <sup>34</sup>D. Surblys, H. Matsubara, G. Kikugawa, and T. Ohara, "Application of atomic stress to compute heat flux via molecular dynamics for systems with many-body interactions," *Phys. Rev. E* **99**, 051301 (2019).
- <sup>35</sup>D. Tisi, L. Zhang, R. Bertossa, H. Wang, R. Car, and S. Baroni, "Heat transport in liquid water from first-principles and deep neural network simulations," *Phys. Rev. B* **104**, 224202 (2021).
- <sup>36</sup>N. Artrith and A. Urban, "An implementation of artificial neural-network potentials for atomistic materials simulations: Performance for TiO<sub>2</sub>," *Comput. Mater. Sci.* **114**, 135–150 (2016).
- <sup>37</sup>K. Shimamura, Y. Takeshita, S. Fukushima, A. Koura, and F. Shimojo, "Computational and training requirements for interatomic potential based on artificial neural network for estimating low thermal conductivity of silver chalcogenides," *J. Chem. Phys.* **153**, 234301 (2020).
- <sup>38</sup>D. Tisi, F. Grasselli, L. Gigli, and M. Cieriotti, "Thermal transport of Li<sub>3</sub>PS<sub>4</sub> solid electrolytes with ab initio accuracy" (2024), [arXiv:2401.12936](https://arxiv.org/abs/2401.12936) [cond-mat.mtrl-sci].
- <sup>39</sup>A. P. Bartók, R. Kondor, and G. Csányi, "On representing chemical environments," *Phys. Rev. B* **87**, 184115 (2013).
- <sup>40</sup><sup>MLIP</sup>, "Gitlab repository, see <https://gitlab.com/ashapeev/mlip-2>" (2024) (last accessed Jan 18, 2024).
- <sup>41</sup>M. F. Langer, F. Knoop, C. Carbogno, M. Scheffler, and M. Rupp, "Heat flux for semilocal machine-learning potentials," *Phys. Rev. B* **108**, L100302 (2023).
- <sup>42</sup>M. F. Langer, J. T. Frank, and F. Knoop, "Stress and heat flux via automatic differentiation," *J. Chem. Phys.* **159**, 174105 (2023).
- <sup>43</sup>B. C. Daly and H. J. Maris, "Calculation of the thermal conductivity of superlattices by molecular dynamics simulation," *Phys. B: Condens. Matter* **316–317**, 247–249 (2002).
- <sup>44</sup>B. C. Daly, H. J. Maris, K. Imamura, and S. Tamura, "Molecular dynamics calculation of the thermal conductivity of superlattices," *Phys. Rev. B* **66**, 024301 (2002).
- <sup>45</sup>E. Lampin, P. L. Palla, P.-A. Francioso, and F. Cleri, "Thermal conductivity from approach-to-equilibrium molecular dynamics," *J. Appl. Phys.* **114**, 033525 (2013).
- <sup>46</sup>R. Kubo, "Statistical-mechanical theory of irreversible processes. I. General theory and simple applications to magnetic and conduction problems," *J. Phys. Soc. Jpn.* **12**, 570–586 (1957).
- <sup>47</sup>A. J. C. Ladd, B. Moran, and W. G. Hoover, "Lattice thermal conductivity: A comparison of molecular dynamics and anharmonic lattice dynamics," *Phys. Rev. B* **34**, 5058–5064 (1986).
- <sup>48</sup>S. Chen, Y. Zhang, J. Wang, and H. Zhao, "Finite-size effects on current correlation functions," *Phys. Rev. E* **89**, 022111 (2014).
- <sup>49</sup>Z. Wang and X. Ruan, "On the domain size effect of thermal conductivities from equilibrium and nonequilibrium molecular dynamics simulations," *J. Appl. Phys.* **121**, 044301 (2017).
- <sup>50</sup>K. Xu, Z. Fan, J. Zhang, N. Wei, and T. Ala-Nissila, "Thermal transport properties of single-layer black phosphorus from extensive molecular dynamics simulations," *Modell. Simul. Mater. Sci. Eng.* **26**, 085001 (2018).
- <sup>51</sup>S. Nosé, "A unified formulation of the constant temperature molecular dynamics methods," *J. Chem. Phys.* **81**, 511–519 (1984).
- <sup>52</sup>W. G. Hoover, "Canonical dynamics: Equilibrium phase-space distributions," *Phys. Rev. A* **31**, 1695–1697 (1985).
- <sup>53</sup>Z. Li, S. Xiong, C. Sievers, Y. Hu, Z. Fan, N. Wei, H. Bao, S. Chen, D. Donadio, and T. Ala-Nissila, "Influence of thermostatting on nonequilibrium molecular dynamics simulations of heat conduction in solids," *J. Chem. Phys.* **151**, 234105 (2019).
- <sup>54</sup>Z. Fan, H. Dong, A. Harju, and T. Ala-Nissila, "Homogeneous nonequilibrium molecular dynamics method for heat transport and spectral decomposition with many-body potentials," *Phys. Rev. B* **99**, 064308 (2019).
- <sup>55</sup>Z. Fan, L. F. C. Pereira, P. Hirvonen, M. M. Ervasti, K. R. Elder, D. Donadio, T. Ala-Nissila, and A. Harju, "Thermal conductivity decomposition in two-

dimensional materials: Application to graphene," *Phys. Rev. B* **95**, 144309 (2017).

<sup>56</sup>K. Sääskilähti, J. Oksanen, J. Tulkki, and S. Volz, "Role of anharmonic phonon scattering in the spectrally decomposed thermal conductance at planar interfaces," *Phys. Rev. B* **90**, 134312 (2014).

<sup>57</sup>K. Sääskilähti, J. Oksanen, S. Volz, and J. Tulkki, "Frequency-dependent phonon mean free path in carbon nanotubes from nonequilibrium molecular dynamics," *Phys. Rev. B* **91**, 115426 (2015).

<sup>58</sup>W. Lv and A. Henry, "Direct calculation of modal contributions to thermal conductivity via Green–Kubo modal analysis," *New J. Phys.* **18**, 013028 (2016).

<sup>59</sup>A. J. Gabourie, Z. Fan, T. Ala-Nissila, and E. Pop, "Spectral decomposition of thermal conductivity: Comparing velocity decomposition methods in homogeneous molecular dynamics simulations," *Phys. Rev. B* **103**, 205421 (2021).

<sup>60</sup>R. Jinnouchi, J. Lahnsteiner, F. Karsai, G. Kresse, and M. Bokdam, "Phase transitions of hybrid perovskites simulated by machine-learning force fields trained on the fly with Bayesian inference," *Phys. Rev. Lett.* **122**, 225701 (2019).

<sup>61</sup>K. Schütt, P.-J. Kindermans, H. E. Sauceda Felix, S. Chmiela, A. Tkatchenko, and K.-R. Müller, "SchNet: A continuous-filter convolutional neural network for modeling quantum interactions," in *Advances in Neural Information Processing Systems*, Vol. 30, edited by I. Guyon, U. V. Luxburg, S. Bengio, H. Wallach, R. Fergus, S. Vishwanathan, and R. Garnett (Curran Associates, Inc., 2017).

<sup>62</sup>T. Frank, O. Unke, and K.-R. Müller, "So3krates: Equivariant attention for interactions on arbitrary length-scales in molecular systems," in *Advances in Neural Information Processing Systems*, Vol. 35, edited by S. Koyejo, S. Mohamed, A. Agarwal, D. Belgrave, K. Cho, and A. Oh (Curran Associates, Inc., 2022), pp. 29400–29413.

<sup>63</sup>M. Wen, Y. Afshar, R. S. Elliott, and E. B. Tadmor, "KLIF: A framework to develop physics-based and machine learning interatomic potentials," *Comput. Phys. Commun.* **272**, 108218 (2022).

<sup>64</sup>G. C. Sosso, D. Donadio, S. Caravati, J. Behler, and M. Bernasconi, "Thermal transport in phase-change materials from atomistic simulations," *Phys. Rev. B* **86**, 104301 (2012).

<sup>65</sup>D. Campi, D. Donadio, G. C. Sosso, J. Behler, and M. Bernasconi, "Electron-phonon interaction and thermal boundary resistance at the crystal-amorphous interface of the phase change compound GeTe," *J. Appl. Phys.* **117**, 015304 (2015).

<sup>66</sup>E. Bosoni, D. Campi, D. Donadio, G. C. Sosso, J. Behler, and M. Bernasconi, "Atomistic simulations of thermal conductivity in GeTe nanowires," *J. Phys. D: Appl. Phys.* **53**, 054001 (2019).

<sup>67</sup>M. Wen and E. B. Tadmor, "Hybrid neural network potential for multilayer graphene," *Phys. Rev. B* **100**, 195419 (2019).

<sup>68</sup>B. Cheng and D. Frenkel, "Computing the heat conductivity of fluids from density fluctuations," *Phys. Rev. Lett.* **125**, 130602 (2020).

<sup>69</sup>C. Mangold, S. Chen, G. Barbalinardo, J. Behler, P. Pochet, K. Termentzidis, Y. Han, L. Chaput, D. Lacroix, and D. Donadio, "Transferability of neural network potentials for varying stoichiometry: Phonons and thermal conductivity of Mn<sub>x</sub>Ge<sub>1-x</sub> compounds," *J. Appl. Phys.* **127**, 244901 (2020).

<sup>70</sup>L. Han, X. Chen, Q. Wang, Y. Chen, M. Xu, L. Wu, C. Chen, P. Lu, and P. Guan, "Neural network potential for studying the thermal conductivity of Sn," *Comput. Mater. Sci.* **200**, 110829 (2021).

<sup>71</sup>K. Shimamura, Y. Takeshita, S. Fukushima, A. Koura, and F. Shimojo, "Estimating thermal conductivity of  $\alpha$ -Ag<sub>2</sub>Se using ANN potential with Chebyshev descriptor," *Chem. Phys. Lett.* **778**, 138748 (2021).

<sup>72</sup>Y. Takeshita, K. Shimamura, S. Fukushima, A. Koura, and F. Shimojo, "Thermal conductivity calculation based on Green–Kubo formula using ANN potential for  $\beta$ -Ag<sub>2</sub>Se," *J. Phys. Chem. Solids* **163**, 110580 (2022).

<sup>73</sup>K. Shimamura, A. Koura, and F. Shimojo, "Construction of machine-learning interatomic potential under heat flux regularization and its application to power spectrum analysis for silver chalcogenides," *Comput. Phys. Commun.* **294**, 108920 (2024).

<sup>74</sup>X. Qian, S. Peng, X. Li, Y. Wei, and R. Yang, "Thermal conductivity modeling using machine learning potentials: Application to crystalline and amorphous silicon," *Mater. Today Phys.* **10**, 100140 (2019).

<sup>75</sup>C. Zhang and Q. Sun, "Gaussian approximation potential for studying the thermal conductivity of silicene," *J. Appl. Phys.* **126**, 105103 (2019).

<sup>76</sup>Z. Zeng, C. Zhang, Y. Xia, Z. Fan, C. Wolverton, and Y. Chen, "Nonperturbative phonon scatterings and the two-channel thermal transport in Tl<sub>3</sub>VSe<sub>4</sub>," *Phys. Rev. B* **103**, 224307 (2021).

<sup>77</sup>X. Gu and C. Zhao, "Thermal conductivity of single-layer MoS<sub>2(1-x)</sub>Se<sub>2x</sub> alloys from molecular dynamics simulations with a machine-learning-based interatomic potential," *Comput. Mater. Sci.* **165**, 74–81 (2019).

<sup>78</sup>P. Korotaev, I. Novoselov, A. Yanilkin, and A. Shapeev, "Accessing thermal conductivity of complex compounds by machine learning interatomic potentials," *Phys. Rev. B* **100**, 144308 (2019).

<sup>79</sup>H. Liu, X. Qian, H. Bao, C. Y. Zhao, and X. Gu, "High-temperature phonon transport properties of SnSe from machine-learning interatomic potential," *J. Phys.: Condens. Matter* **33**, 405401 (2021).

<sup>80</sup>H. Yang, Y. Zhu, E. Dong, Y. Wu, J. Yang, and W. Zhang, "Dual adaptive sampling and machine learning interatomic potentials for modeling materials with chemical bond hierarchy," *Phys. Rev. B* **104**, 094310 (2021).

<sup>81</sup>Z. Zeng, C. Zhang, H. Yu, W. Li, Y. Pei, and Y. Chen, "Ultralow and glass-like lattice thermal conductivity in crystalline BaAg<sub>2</sub>Te<sub>2</sub>: Strong fourth-order anharmonicity and crucial diffusive thermal transport," *Mater. Today Phys.* **21**, 100487 (2021).

<sup>82</sup>S. Attarian, D. Morgan, and I. Szlufarska, "Thermophysical properties of flibe using moment tensor potentials," *J. Mol. Liq.* **368**, 120803 (2022).

<sup>83</sup>N. Ouyang, C. Wang, and Y. Chen, "Temperature- and pressure-dependent phonon transport properties of SnS across phase transition from machine-learning interatomic potential," *Int. J. Heat Mass Transfer* **192**, 122859 (2022).

<sup>84</sup>Y. Ouyang, C. Yu, J. He, P. Jiang, W. Ren, and J. Chen, "Accurate description of high-order phonon anharmonicity and lattice thermal conductivity from molecular dynamics simulations with machine learning potential," *Phys. Rev. B* **105**, 115202 (2022).

<sup>85</sup>B. Mortazavi and X. Zhuang, "Ultrahigh strength and negative thermal expansion and low thermal conductivity in graphyne nanosheets confirmed by machine-learning interatomic potentials," *FlatChem* **36**, 100446 (2022).

<sup>86</sup>B. Mortazavi, F. Shojaei, M. Yagmurcukardes, A. V. Shapeev, and X. Zhuang, "Anisotropic and outstanding mechanical, thermal conduction, optical, and piezoelectric responses in a novel semiconducting bcn monolayer confirmed by first-principles and machine learning," *Carbon* **200**, 500–509 (2022).

<sup>87</sup>B. Mortazavi and X. Zhuang, "Low and anisotropic tensile strength and thermal conductivity in the single-layer fullerene network predicted by machine-learning interatomic potentials," *Coatings* **12**, 1171 (2022).

<sup>88</sup>J. Sun, M. Hu, C. Zhang, L. Bai, C. Zhang, and Q. Wang, "Ultralow thermal conductivity of layered Bi<sub>2</sub>O<sub>2</sub>Se induced by twisting," *Adv. Funct. Mater.* **32**, 2209000 (2022).

<sup>89</sup>B. Mortazavi, "Structural, electronic, thermal and mechanical properties of C<sub>60</sub>-based fullerene two-dimensional networks explored by first-principles and machine learning," *Carbon* **213**, 118293 (2023).

<sup>90</sup>B. Mortazavi, F. Shojaei, and X. Zhuang, "A novel two-dimensional C<sub>36</sub> fullerene network: An isotropic, auxetic semiconductor with low thermal conductivity and remarkable stiffness," *Mater. Today Nano* **21**, 100280 (2023).

<sup>91</sup>B. Mortazavi, Y. Rémond, H. Fang, T. Rabczuk, and X. Zhuang, "Hexagonal boron–carbon fullerene heterostructures: Stable two-dimensional semiconductors with remarkable stiffness, low thermal conductivity and flat bands," *Mater. Today Commun.* **36**, 106856 (2023).

<sup>92</sup>Q. Wang, Z. Zeng, P. Zhao, C. Chen, N. Ouyang, J. Mao, and Y. Chen, "B-site columnar-ordered halide double perovskites: Breaking octahedra motions induces strong lattice anharmonicity and thermal anisotropy," *Chem. Mater.* **35**, 1633–1639 (2023).

<sup>93</sup>Y. Zhu, E. Dong, H. Yang, L. Xi, J. Yang, and W. Zhang, "Atomic potential energy uncertainty in machine-learning interatomic potentials and thermal transport in solids with atomic diffusion," *Phys. Rev. B* **108**, 014108 (2023).

<sup>94</sup>C.-M. Chang, "Exploring thermal properties of PbSnTeSe and PbSnTeS high entropy alloys with machine-learned potentials," *Modell. Simul. Mater. Sci. Eng.* **32**, 035008 (2024).



- <sup>95</sup>S. Wieser and E. Zojer, "Machine learned force-fields for an *ab-initio* quality description of metal-organic frameworks," *npj Comput. Mater.* **10**, 18 (2024).
- <sup>96</sup>F.-Z. Dai, B. Wen, Y. Sun, H. Xiang, and Y. Zhou, "Theoretical prediction on thermal and mechanical properties of high entropy ( $\text{Zr}_{0.2}\text{Hf}_{0.2}\text{Ti}_{0.2}\text{Nb}_{0.2}\text{Ta}_{0.2}$ )C by deep learning potential," *J. Mater. Sci. Technol.* **43**, 168–174 (2020).
- <sup>97</sup>R. Li, Z. Liu, A. Rohskopf, K. Gordiz, A. Henry, E. Lee, and T. Luo, "A deep neural network interatomic potential for studying thermal conductivity of  $\beta\text{-Ga}_2\text{O}_3$ ," *Appl. Phys. Lett.* **117**, 152102 (2020).
- <sup>98</sup>R. Li, E. Lee, and T. Luo, "A unified deep neural network potential capable of predicting thermal conductivity of silicon in different phases," *Mater. Today Phys.* **12**, 100181 (2020).
- <sup>99</sup>G. Pan, P. Chen, H. Yan, and Y. Lu, "A DFT accurate machine learning description of molten  $\text{ZnCl}_2$  and its mixtures: 1. Potential development and properties prediction of molten  $\text{ZnCl}_2$ ," *Comput. Mater. Sci.* **185**, 109955 (2020).
- <sup>100</sup>M. Bu, W. Liang, G. Lu, and J. Yu, "Local structure elucidation and properties prediction on  $\text{KCl}\text{-CaCl}_2$  molten salt: A deep potential molecular dynamics study," *Sol. Energy Mater. Sol. Cells* **232**, 111346 (2021).
- <sup>101</sup>F.-Z. Dai, Y. Sun, B. Wen, H. Xiang, and Y. Zhou, "Temperature dependent thermal and elastic properties of high entropy ( $\text{Ti}_{0.2}\text{Zr}_{0.2}\text{Hf}_{0.2}\text{Nb}_{0.2}\text{Ta}_{0.2}$ )B<sub>2</sub>: Molecular dynamics simulation by deep learning potential," *J. Mater. Sci. Technol.* **72**, 8–15 (2021).
- <sup>102</sup>J. Deng and L. Stixrude, "Thermal conductivity of silicate liquid determined by machine learning potentials," *Geophys. Res. Lett.* **48**, e2021GL093806, <https://doi.org/10.1029/2021GL093806> (2021).
- <sup>103</sup>Q. Liu, J. Li, and M. Chen, "Thermal transport by electrons and ions in warm dense aluminum: A combined density functional theory and deep potential study," *Matter Radiat. Extremes* **6**, 026902 (2021).
- <sup>104</sup>M. K. Gupta, J. Ding, D. Bansal, D. L. Abernathy, G. Ehlers, N. C. Osti, W. G. Zeier, and O. Delaire, "Strongly anharmonic phonons and their role in superionic diffusion and ultralow thermal conductivity of  $\text{Cu}_7\text{PSe}_6$ ," *Adv. Energy Mater.* **12**, 2200596 (2022).
- <sup>105</sup>X. Huang, Y. Shen, and Q. An, "Nanotwinning induced decreased lattice thermal conductivity of high temperature thermoelectric boron subphosphide ( $\text{B}_{12}\text{P}_2$ ) from deep learning potential simulations," *Energy and AI* **8**, 100135 (2022).
- <sup>106</sup>W. Liang, G. Lu, and J. Yu, "Machine learning accelerates molten salt simulations: Thermal conductivity of  $\text{MgCl}_2\text{-NaCl}$  eutectic," *Adv. Theory Simul.* **5**, 2200206 (2022).
- <sup>107</sup>P. Pegolo, S. Baroni, and F. Grasselli, "Temperature-and vacancy-concentration-dependence of heat transport in  $\text{Li}_3\text{ClO}$  from multi-method numerical simulations," *npj Comput. Mater.* **8**, 24 (2022).
- <sup>108</sup>D. Wang, Z. Wu, and X. Deng, "Thermal conductivity of hydrous wadsleyite determined by non-equilibrium molecular dynamics based on machine learning," *Geophys. Res. Lett.* **49**, e2022GL100337, <https://doi.org/10.1029/2022GL100337> (2022).
- <sup>109</sup>F. Yang, Q. Zeng, B. Chen, D. Kang, S. Zhang, J. Wu, X. Yu, and J. Dai, "Lattice thermal conductivity of  $\text{MgSiO}_3$  perovskite and post-perovskite under lower mantle conditions calculated by deep potential molecular dynamics," *Chin. Phys. Lett.* **39**, 116301 (2022).
- <sup>110</sup>P. Zhang, Z. Zhang, Y. Liu, Z. Wang, Z. Lu, and R. Xiong, "Phonon thermal transport in  $\text{Bi}_2\text{Te}_3$  from a deep-neural-network interatomic potential," *Phys. Rev. Appl.* **18**, 054022 (2022).
- <sup>111</sup>N. Bhatt, P. Karna, S. Thakur, and A. Giri, "Transition from electron-dominated to phonon-driven thermal transport in tungsten under extreme pressures," *Phys. Rev. Mater.* **7**, 115001 (2023).
- <sup>112</sup>W. Dong, H. Tian, W. Zhang, J.-J. Zhou, and X. Pang, "Development of  $\text{NaCl-MgCl}_2\text{-CaCl}_2$  ternary salt for high-temperature thermal energy storage using machine learning," *ACS Appl. Mater. Interfaces* **16**, 530–539 (2024).
- <sup>113</sup>S. Fu, D. Liu, Y. Deng, M. Li, H. Zhao, J. Guo, J. Zhou, P. Zhang, C. Wang, H. Yu, and S. Dang, "Medium-entropy ceramic aerogels for robust thermal sealing," *J. Mater. Chem. A* **11**, 742–752 (2023).
- <sup>114</sup>M. K. Gupta, S. Kumar, R. Mittal, S. K. Mishra, S. Rols, O. Delaire, A. Thamizhavel, P. Sastry, and S. L. Chaplot, "Distinct anharmonic characteristics of phonon-driven lattice thermal conductivity and thermal expansion in bulk  $\text{MoSe}_2$  and  $\text{WSe}_2$ ," *J. Mater. Chem. A* **11**, 21864–21873 (2023).
- <sup>115</sup>J. Han, Q. Zeng, K. Chen, X. Yu, and J. Dai, "Lattice thermal conductivity of monolayer InSe calculated by machine learning potential," *Nanomaterials* **13**, 1576 (2023).
- <sup>116</sup>X. Huang, K. Luo, Y. Shen, Y. Yue, and Q. An, "Grain boundaries induce significant decrease in lattice thermal conductivity of CdTe," *Energy AI* **11**, 100210 (2023).
- <sup>117</sup>Z. Li, X. Tan, Z. Fu, L. Liu, and J.-Y. Yang, "Thermal transport across copper–water interfaces according to deep potential molecular dynamics," *Phys. Chem. Chem. Phys.* **25**, 6746–6756 (2023).
- <sup>118</sup>Z. Li, J. Wang, C. Yang, L. Liu, and J.-Y. Yang, "Thermal transport across  $\text{TiO}_2\text{-H}_2\text{O}$  interface involving water dissociation: *Ab initio*-assisted deep potential molecular dynamics," *J. Chem. Phys.* **159**, 144701 (2023).
- <sup>119</sup>Y. Qi, X. Guo, H. Wang, S. Zhang, M. Li, P. Zhou, and D. Guo, "Reversible densification and cooperative atomic movement induced 'Compaction' in vitreous silica: A new sight from deep neural network interatomic potentials," *J. Mater. Sci.* **58**, 9515–9532 (2023).
- <sup>120</sup>R. Qiu, Q. Zeng, H. Wang, D. Kang, X. Yu, and J. Dai, "Anomalous thermal transport across the superionic transition in ice," *Chin. Phys. Lett.* **40**, 116301 (2023).
- <sup>121</sup>R. Qu, Y. Lv, and Z. Lu, "A deep neural network potential to study the thermal conductivity of  $\text{MnBi}_2\text{Te}_4$  and  $\text{Bi}_2\text{Te}_3/\text{MnBi}_2\text{Te}_4$  superlattice," *J. Electron. Mater.* **52**, 4475–4483 (2023).
- <sup>122</sup>Q. Ren, M. K. Gupta, M. Jin, J. Ding, J. Wu, Z. Chen, S. Lin, O. Fabelo, J. A. Rodríguez-Velamazán, M. Kofu, and K. Nakajima, "Extreme phonon anharmonicity underpins superionic diffusion and ultralow thermal conductivity in argyrodite  $\text{Ag}_8\text{SnSe}_6$ ," *Nat. Mater.* **22**, 999–1006 (2023).
- <sup>123</sup>D. Wang, Z. Wu, and X. Deng, "Thermal conductivity of Fe-bearing bridgmanite and post-perovskite: Implications for the heat flux from the core," *Earth Planet. Sci. Lett.* **621**, 118368 (2023).
- <sup>124</sup>T. Xu, X. Li, Y. Wang, and Z. Tang, "Development of deep potentials of molten  $\text{MgCl}_2\text{-NaCl}$  and  $\text{MgCl}_2\text{-KCl}$  salts driven by machine learning," *ACS Appl. Mater. Interfaces* **15**, 14184–14195 (2023).
- <sup>125</sup>P. Zhang, W. Liao, Z. Zhu, M. Qin, Z. Zhang, D. Jin, Y. Liu, Z. Wang, Z. Lu, and R. Xiong, "Tuning the lattice thermal conductivity of  $\text{Sb}_2\text{Te}_3$  by Cr doping: A deep potential molecular dynamics study," *Phys. Chem. Chem. Phys.* **25**, 15422–15432 (2023).
- <sup>126</sup>P. Zhang, M. Qin, Z. Zhang, D. Jin, Y. Liu, Z. Wang, Z. Lu, J. Shi, and R. Xiong, "Accessing the thermal conductivities of  $\text{Sb}_2\text{Te}_3$  and  $\text{Bi}_2\text{Te}_3/\text{Sb}_2\text{Te}_3$  superlattices by molecular dynamics simulations with a deep neural network potential," *Phys. Chem. Chem. Phys.* **25**, 6164–6174 (2023).
- <sup>127</sup>C. Zhang, M. Puligheddu, L. Zhang, R. Car, and G. Galli, "Thermal conductivity of water at extreme conditions," *J. Phys. Chem. B* **127**, 7011–7017 (2023).
- <sup>128</sup>J. Zhang, H. Zhang, J. Wu, X. Qian, B. Song, C.-T. Lin, T.-H. Liu, and R. Yang, "Vacancy-induced phonon localization in boron arsenide using a unified neural network interatomic potential," *Cell Rep. Phys. Sci.* **5**, 101760 (2024).
- <sup>129</sup>C. Zhao, Y. Tao, and Y. He, "Microstructure and thermophysical property prediction for chloride composite phase change materials: A deep potential molecular dynamics study," *J. Phys. Chem. C* **127**, 6852–6860 (2023).
- <sup>130</sup>B. Fu, Y. Sun, W. Jiang, F. Wang, L. Zhang, H. Wang, and B. Xu, "Determining the thermal conductivity and phonon behavior of SiC materials with quantum accuracy via deep learning interatomic potential model," *J. Nucl. Mater.* **591**, 154897 (2024).
- <sup>131</sup>T. Li, Q. Hou, J.-C. Cui, J.-H. Yang, B. Xu, M. Li, J. Wang, and B.-Q. Fu, "Deep learning interatomic potential for thermal and defect behaviour of aluminum nitride with quantum accuracy," *Comput. Mater. Sci.* **232**, 112656 (2024).
- <sup>132</sup>R. Li, K. Hussain, M. E. Liao, K. Huynh, M. S. B. Hoque, S. Wyant, Y. R. Koh, Z. Xu, Y. Wang, D. P. Luccioni, Z. Cheng, J. Shi, E. Lee, S. Graham, A. Henry, P. E. Hopkins, M. S. Goorsky, M. Khan, and T. Luo, "Enhanced

thermal boundary conductance across GaN/SiC interfaces with AlN transition layers,” *ACS Appl. Mater. Interfaces* **16**, 8109–8118 (2024).

<sup>135</sup>Y. Peng and J. Deng, “Thermal conductivity of MgSiO<sub>3</sub>-H<sub>2</sub>O system determined by machine learning potentials,” *Geophys. Res. Lett.* **51**, e2023GL107245 (2024).

<sup>136</sup>H. Zhang, G. Ren, P. Jia, X. Zhao, and N. Ni, “Development of machine learning force field for thermal conductivity analysis in MoAlB: Insights into anisotropic heat transfer mechanisms,” *Ceram. Int.* **50**, 13740–13749 (2024).

<sup>137</sup>C. Verdi, F. Karsai, P. Liu, R. Jinnouchi, and G. Kresse, “Thermal transport and phase transitions of zirconia by on-the-fly machine-learned interatomic potentials,” *npj Comput. Mater.* **7**, 156 (2021).

<sup>138</sup>J. Lahnsteiner, M. Rang, and M. Bokdam, “Tuning einstein oscillator frequencies of cation rattlers: A molecular dynamics study of the lattice thermal conductivity of CsPbBr<sub>3</sub>,” *J. Phys. Chem. C* **128**, 1341–1349 (2024).

<sup>139</sup>H. Dong, Z. Fan, P. Qian, and Y. Su, “Exactly equivalent thermal conductivity in finite systems from equilibrium and nonequilibrium molecular dynamics simulations,” *Phys. E: Low-Dimens. Syst. Nanostruct.* **144**, 115410 (2022).

<sup>140</sup>R. Cheng, X. Shen, S. Klotz, Z. Zeng, Z. Li, A. Ivanov, Y. Xiao, L.-D. Zhao, F. Weber, and Y. Chen, “Lattice dynamics and thermal transport of PbTe under high pressure,” *Phys. Rev. B* **108**, 104306 (2023).

<sup>141</sup>H. Dong, C. Cao, P. Ying, Z. Fan, P. Qian, and Y. Su, “Anisotropic and high thermal conductivity in monolayer quasi-hexagonal fullerene: A comparative study against bulk phase fullerene,” *Int. J. Heat Mass Transfer* **206**, 123943 (2023).

<sup>142</sup>P.-H. Du, C. Zhang, T. Li, and Q. Sun, “Low lattice thermal conductivity with two-channel thermal transport in the superatomic crystal PH<sub>4</sub>AlBr<sub>4</sub>,” *Phys. Rev. B* **107**, 155204 (2023).

<sup>143</sup>F. Eriksson, E. Fransson, C. Linderålv, Z. Fan, and P. Erhart, “Tuning the through-plane lattice thermal conductivity in van der Waals structures through rotational (DIS) ordering,” *ACS Nano* **17**, 25565–25574 (2023).

<sup>144</sup>T. Liang, P. Ying, K. Xu, Z. Ye, C. Ling, Z. Fan, and J. Xu, “Mechanisms of temperature-dependent thermal transport in amorphous silica from machine-learning molecular dynamics,” *Phys. Rev. B* **108**, 184203 (2023).

<sup>145</sup>Y. Liu, Y. Liu, J. Yue, L. Xiong, L.-L. Nian, and S. Hu, “Modulation of interface modes for resonance-induced enhancement of the interfacial thermal conductance in pillar-based Si/Ge nanowires,” *Phys. Rev. B* **108**, 235426 (2023).

<sup>146</sup>Y. Lu, Y. Shi, J. Wang, H. Dong, and J. Yu, “Reduction of thermal conductivity in carbon nanotubes by fullerene encapsulation from machine-learning molecular dynamics simulations,” *J. Appl. Phys.* **134**, 244901 (2023).

<sup>147</sup>N. Ouyang, Z. Zeng, C. Wang, Q. Wang, and Y. Chen, “Role of high-order lattice anharmonicity in the phonon thermal transport of silver halide Ag X (X = Cl, Br, I),” *Phys. Rev. B* **108**, 174302 (2023).

<sup>148</sup>S. Pan, T. Huang, A. Vazan, Z. Liang, C. Liu, J. Wang, C. J. Pickard, H.-T. Wang, D. Xing, and J. Sun, “Magnesium oxide-water compounds at megabar pressure and implications on planetary interiors,” *Nat. Commun.* **14**, 1165 (2023).

<sup>149</sup>W. Sha, X. Dai, S. Chen, B. Yin, and F. Guo, “Phonon thermal transport in two-dimensional PbTe monolayers via extensive molecular dynamics simulations with a neuroevolution potential,” *Mater. Today Phys.* **34**, 101066 (2023).

<sup>150</sup>Y.-B. Shi, Y.-Y. Chen, H. Wang, S. Cao, Y.-X. Zhu, M.-F. Chu, Z.-F. Shao, H.-K. Dong, and P. Qian, “Investigation of the mechanical and transport properties of InGeX<sub>3</sub> (X = S, Se and Te) monolayers using density functional theory and machine learning,” *Phys. Chem. Chem. Phys.* **25**, 13864–13876 (2023).

<sup>151</sup>Y. Shi, Y. Chen, H. Dong, H. Wang, and P. Qian, “Investigation of phase transition, mechanical behavior and lattice thermal conductivity of halogen perovskites using machine learning interatomic potentials,” *Phys. Chem. Chem. Phys.* **25**, 30644–30655 (2023).

<sup>152</sup>Y. Su, Y.-Y. Chen, H. Wang, H.-K. Dong, S. Cao, L.-B. Shi, and P. Qian, “Origin of low lattice thermal conductivity and mobility of lead-free halide double perovskites,” *J. Alloys Compd.* **962**, 170988 (2023).

<sup>153</sup>Z. Sun, Z. Qi, K. Liang, X. Sun, Z. Zhang, L. Li, Q. Wang, G. Zhang, G. Wu, and W. Shen, “A neuroevolution potential for predicting the thermal conductivity of  $\alpha$ ,  $\beta$ , and  $\epsilon$ -Ga<sub>2</sub>O<sub>3</sub>,” *Appl. Phys. Lett.* **123**, 192202 (2023).

<sup>154</sup>Y. Wang, Z. Fan, P. Qian, M. A. Caro, and T. Ala-Nissila, “Quantum-corrected thickness-dependent thermal conductivity in amorphous silicon predicted by machine learning molecular dynamics simulations,” *Phys. Rev. B* **107**, 054303 (2023).

<sup>155</sup>Q. Wang, C. Wang, C. Chi, N. Ouyang, R. Guo, N. Yang, and Y. Chen, “Phonon transport in freestanding SrTiO<sub>3</sub> down to the monolayer limit,” *Phys. Rev. B* **108**, 115435 (2023).

<sup>156</sup>K. Xu, Y. Hao, T. Liang, P. Ying, J. Xu, J. Wu, and Z. Fan, “Accurate prediction of heat conductivity of water by a neuroevolution potential,” *J. Chem. Phys.* **158**, 204114 (2023).

<sup>157</sup>J. Xiong, Z. Qi, K. Liang, X. Sun, Z. Sun, Q. Wang, L. Chen, G. Wu, and W. Shen, “Molecular dynamics insights on thermal conductivities of cubic diamond, lonsdaleite and nanotwinned diamond via the machine learned potential,” *Chin. Phys. B* **32**, 128101 (2023).

<sup>158</sup>P. Ying, T. Liang, K. Xu, J. Zhang, J. Xu, Z. Zhong, and Z. Fan, “Sub-micrometer phonon mean free paths in metal-organic frameworks revealed by machine-learning molecular dynamics simulations,” *ACS Appl. Mater. Interfaces* **15**, 36412–36422 (2023).

<sup>159</sup>P. Ying, T. Liang, K. Xu, J. Xu, Z. Fan, T. Ala-Nissila, and Z. Zhong, “Variable thermal transport in black, blue, and violet phosphorene from extensive atomistic simulations with a neuroevolution potential,” *Int. J. Heat Mass Transfer* **202**, 123681 (2023).

<sup>160</sup>H. Zhang, X. Gu, Z. Fan, and H. Bao, “Vibrational anharmonicity results in decreased thermal conductivity of amorphous HfO<sub>2</sub> at high temperature,” *Phys. Rev. B* **108**, 045422 (2023).

<sup>161</sup>C. Cao, S. Cao, Y. Zhu, H. Dong, Y. Wang, and P. Qian, “Thermal transports of 2D phosphorous carbides by machine learning molecular dynamics simulations,” *Int. J. Heat Mass Transfer* **224**, 125359 (2024).

<sup>162</sup>R. Cheng, Z. Zeng, C. Wang, N. Ouyang, and Y. Chen, “Impact of strain-insensitive low-frequency phonon modes on lattice thermal transport in A<sub>2</sub>XB<sub>6</sub>-type perovskites,” *Phys. Rev. B* **109**, 054305 (2024).

<sup>163</sup>H. Fan, P. Ying, Z. Fan, Y. Chen, Z. Li, and Y. Zhou, “Anomalous strain-dependent thermal conductivity in the metal-organic framework HKUST-1,” *Phys. Rev. B* **109**, 045424 (2024).

<sup>164</sup>Z. Fan, Y. Xiao, Y. Wang, P. Ying, S. Chen, and H. Dong, “Combining linear-scaling quantum transport and machine-learning molecular dynamics to study thermal and electronic transports in complex materials,” *J. Phys.: Condens. Matter* **36**, 245901 (2024).

<sup>165</sup>G. Li, J. Tang, J. Zheng, Q. Wang, Z. Cui, K. Xu, J. Xu, T.-H. Liu, G. Zhu, R. Guo, and B. Li, “Convergent thermal conductivity in strained monolayer graphene,” *Phys. Rev. B* **109**, 035420 (2024).

<sup>166</sup>Y. Li, Y. Guo, S. Xiong, and H. Yi, “Enhanced heat transport in amorphous silicon via microstructure modulation,” *Int. J. Heat Mass Transfer* **222**, 125167 (2024).

<sup>167</sup>Z. Li, H. Dong, J. Wang, L. Liu, and J.-Y. Yang, “Active learning molecular dynamics-assisted insights into ultralow thermal conductivity of two-dimensional covalent organic frameworks,” *Int. J. Heat Mass Transfer* **225**, 125404 (2024).

<sup>168</sup>P. Pegolo and F. Grasselli, “Thermal transport of glasses via machine learning driven simulations,” *Front. Mater.* **11**, 1369034 (2024).

<sup>169</sup>X. Wang, J. Yang, P. Ying, Z. Fan, J. Zhang, and H. Sun, “Dissimilar thermal transport properties in  $\kappa$ -Ga<sub>2</sub>O<sub>3</sub> and  $\beta$ -Ga<sub>2</sub>O<sub>3</sub> revealed by homogeneous non-equilibrium molecular dynamics simulations using machine-learned potentials,” *J. Appl. Phys.* **135**, 065104 (2024).

<sup>170</sup>P. Ying and Z. Fan, “Combining the D3 dispersion correction with the neuroevolution machine-learned potential,” *J. Phys.: Condens. Matter* **36**, 125901 (2023).

<sup>171</sup>J. Yue, S. Hu, B. Xu, R. Chen, L. Xiong, R. Guo, Y. Li, L.-L. Nian, J. Shiomi, and B. Zheng, “Unraveling the mechanisms of thermal boundary conductance at the graphene-silicon interface: Insights from ballistic, diffusive, and localized phonon transport regimes,” *Phys. Rev. B* **109**, 115302 (2024).

<sup>172</sup>M. Zeraati, A. R. Oganov, T. Fan, and S. F. Solodovnikov, “Searching for low thermal conductivity materials for thermal barrier coatings: A theoretical approach,” *Phys. Rev. Mater.* **8**, 033601 (2024).

27 April 2024 04:45:50

- <sup>171</sup>J. Zhang, H.-C. Zhang, W. Li, and G. Zhang, "Thermal conductivity of GeTe crystals based on machine learning potentials," *Chin. Phys. B* **33**, 047402 (2024).
- <sup>172</sup>M. L. Huber, R. A. Perkins, D. G. Friend, J. V. Sengers, M. J. Assael, I. N. Metaxa, K. Miyagawa, R. Hellmann, and E. Vogel, "New international formulation for the thermal conductivity of H<sub>2</sub>O," *J. Phys. Chem. Ref. Data* **41**, 033102 (2012).
- <sup>173</sup>P. Linstrom, see <https://webbook.nist.gov/chemistry/fluid> for "NIST Chemistry WebBook-SRD 69" (2022).
- <sup>174</sup>D. G. Cahill and R. Pohl, "Heat flow and lattice vibrations in glasses," *Solid State Commun.* **70**, 927–930 (1989).
- <sup>175</sup>D. G. Cahill, "Thermal conductivity measurement from 30 to 750 K: The 3 $\omega$  method," *Rev. Sci. Instrum.* **61**, 802–808 (1990).
- <sup>176</sup>K. L. Wray and T. J. Connolly, "Thermal conductivity of clear fused silica at high temperatures," *J. Appl. Phys.* **30**, 1702–1705 (1959).
- <sup>177</sup>B. L. Zink, R. Pietri, and F. Hellman, "Thermal conductivity and specific heat of thin-film amorphous silicon," *Phys. Rev. Lett.* **96**, 055902 (2006).
- <sup>178</sup>C. J. Glassbrenner and G. A. Slack, "Thermal conductivity of silicon and germanium from 3 K to the melting point," *Phys. Rev.* **134**, A1058–A1069 (1964).
- <sup>179</sup>T. Caillat, A. Borshchevsky, and J.-P. Fleurial, "Properties of single crystalline semiconducting CoSb<sub>3</sub>," *J. Appl. Phys.* **80**, 4442–4449 (1996).
- <sup>180</sup>C. Y. Ho, R. W. Powell, and P. E. Liley, "Thermal conductivity of the elements," *J. Phys. Chem. Ref. Data* **1**, 279–421 (1972).
- <sup>181</sup>X. Wu, W. Zhou, H. Dong, P. Ying, Y. Wang, B. Song, Z. Fan, and S. Xiong, "Correcting force error-induced underestimation of lattice thermal conductivity in machine learning molecular dynamics" (2024), [arXiv:2401.11427](https://arxiv.org/abs/2401.11427) [cond-mat.mtrl-sci].
- <sup>182</sup>E. Lindgren, M. Rahm, E. Fransson, F. Eriksson, N. Österbacka, Z. Fan, and P. Erhart, "calorine: A python package for constructing and sampling neuroevolution potential models," *J. Open Source Softw.* **9**, 6264 (2024).
- <sup>183</sup>"GPYUMD," Github repository <https://github.com/AlexGabourie/gpyumd> (2024) (last accessed Jan 18, 2024).
- <sup>184</sup>"GPUMD-WIZARD," Github repository <https://github.com/Jonsnow-willow/GPUMD-Wizard> (2024) (last accessed Jan 18, 2024).
- <sup>185</sup>"PYNEP," Github repository <https://github.com/bigd4/PyNEP> (2024) (last accessed Jan 18, 2024).
- <sup>186</sup>Z. Fan, T. Siro, and A. Harju, "Accelerated molecular dynamics force evaluation on graphics processing units for thermal conductivity calculations," *Comput. Phys. Commun.* **184**, 1414–1425 (2013).
- <sup>187</sup>T. Schaul, T. Glasmachers, and J. Schmidhuber, "High dimensions and heavy tails for natural evolution strategies," in *Proceedings of the 13th Annual Conference on Genetic and Evolutionary Computation*, GECCO '11 (Association for Computing Machinery, New York, NY, 2011), pp. 845–852.
- <sup>188</sup>J. F. Ziegler and J. P. Biersack, "The stopping and range of ions in matter," in *Treatise on Heavy-Ion Science: Volume 6: Astrophysics, Chemistry, and Condensed Matter*, edited by D. A. Bromley (Springer US, Boston, MA, 1985), pp. 93–129.
- <sup>189</sup>S. Grimme, S. Ehrlich, and L. Goerigk, "Effect of the damping function in dispersion corrected density functional theory," *J. Comput. Chem.* **32**, 1456–1465 (2011).
- <sup>190</sup>J. Liu, J. Byggmästar, Z. Fan, P. Qian, and Y. Su, "Large-scale machine-learning molecular dynamics simulation of primary radiation damage in tungsten," *Phys. Rev. B* **108**, 054312 (2023).
- <sup>191</sup>A. M. Miksch, T. Morawietz, J. Kästner, A. Urban, and N. Artrith, "Strategies for the construction of machine-learning potentials for accurate and efficient atomic-scale simulations," *Mach. Learn.: Sci. Technol.* **2**, 031001 (2021).
- <sup>192</sup>A. M. Tokita and J. Behler, "How to train a neural network potential," *J. Chem. Phys.* **159**, 121501 (2023).
- <sup>193</sup>P. E. Blöchl, "Projector augmented-wave method," *Phys. Rev. B* **50**, 17953–17979 (1994).
- <sup>194</sup>J. P. Perdew, K. Burke, and M. Ernzerhof, "Generalized gradient approximation made simple," *Phys. Rev. Lett.* **77**, 3865–3868 (1996).
- <sup>195</sup>J. Tersoff, "Modeling solid-state chemistry: Interatomic potentials for multi-component systems," *Phys. Rev. B* **39**, 5566–5568 (1989).
- <sup>196</sup>A. Togo and I. Tanaka, "First principles phonon calculations in materials science," *Scr. Mater.* **108**, 1–5 (2015).
- <sup>197</sup>H. Dong, Z. Fan, L. Shi, A. Harju, and T. Ala-Nissila, "Equivalence of the equilibrium and the nonequilibrium molecular dynamics methods for thermal conductivity calculations: From bulk to nanowire silicon," *Phys. Rev. B* **97**, 094305 (2018).
- <sup>198</sup>H. R. Shanks, P. D. Maycock, P. H. Sidles, and G. C. Danielson, "Thermal conductivity of silicon from 300 to 1400 K," *Phys. Rev.* **130**, 1743–1748 (1963).
- <sup>199</sup>P. D. Maycock, "Thermal conductivity of silicon, germanium, III–V compounds and III–V alloys," *Solid-State Electron.* **10**, 161–168 (1967).